Modification of ceria with enhanced catalytic properties

Pablo Navarro Acero

BACHELOR'S THESIS IN ENGINEERING PHYSICS

SUPERVISORS:
Dr. Jordi Llorca
Dr. Lluís Soler

Universitat Politècnica de Catalunya
June, 2019
Spain

Contents

Acknowledgments

First of all I would like to give especial thanks to my supervisors: Dr. Jordi Llorca and Dr. Lluís Soler. For their guidance and the dedication shown to me during the last 4 months. Also to the rest of group NEMEN: Núria, Isabel and Xavi. All of them supported me greatly and created a positive environment everyday, which I hope to be able to find again in my future career.

I also need to give thanks to the professors I have had since I started the degree in Engineering Physics. Their effort and dedication has served me as an example I will not forget. And to my friends, from and outside university, which have made the last 4 years easier and been there for me.

And to my Family, without whom I wouldn't be who I am.

Abstract

Ceria has been studied during the last decades due to its unique properties and their corresponding applications. Is an important material in industry, state of the art energy research, optics and biomedicine, among other fields. Advances in synthesis of well-defined nanostructured materials and theoretical studies using computational quantum mechanics have lead to a deeper understanding of the reaction mechanisms at the atomic level. Which has been crucial for the development of enhanced catalysts.

In the first part, this work presents the synthesis, characterization and catalytic test using CO oxidation as probe reaction of different bare ceria samples. After a brief comprehensive introduction to the topic, which in conjuction with the characterization results will provide us with the necessary tools to understand all the experiments outcomes.

The second part consists in the improvement of the catalytic activity of the first samples by depositing AuCu nanoparticles. Which have been used previously on supports other than ceria for CO oxidation and other redox reactions. The results of the characterizations and experiments will provide the key insights into the reaction mechanism in order to establish a reliable relation between catalytic properties and structure. Contributing in this way to the development of enhanced oxide-supported catalysts by elucidating the relevant composition and reaction mechanisms in our case.

Chapter 1

Theoretical background

1.1 Ceria in catalysis

Catalysis is nowadays a well understood phenomenon which plays an essential role in the manufacture of many chemicals and the conduction of many fundamental processes for our society. Its use provides us with technical, ecological and economical viability for many necessary reactions as well as the avoidance of pollutants. Traditionally, three main fields are distinguished in catalysis: heterogeneous, homogeneous and enzymatic. Being the first one the main focus of this work, includes all the reactions in which the catalyst and reactants are in different phases such as solid catalyst and gas reactants.

In heterogeneous catalysis there are reactions which are structure-sensitive. In those cases, the rate of the reaction per surface exposed atom or turnover frequency (TOF) depends on the nature of the exposed surface: crystal planes exposed, the smoothness of the surface... Therefore the control at the nanometer scale of catalysts is desirable for many applications.

Nanostructured ceria is one of the most studied rare earth oxides due to its applications in energy and environmental sciences. Mainly due to its redox and transport properties and for its availability with respect to other rare earths. Cerium is more common in the Earth's crust (66.5 ppm) than that of copper (60 ppm) or tin (2.3 ppm).[1,2] It is used as a promoter in the three-way catalyst (TWCs) for the elimination of toxic exhaust gases, low-temperature water-gas shift reaction, solid oxide fuel cells (SOFC), biomass reforming, UV blocker ...[3–9]

Ceria's stable crystal phase depends on temperature, pressure and O/Ce ratio. CeO_2 crystallizes in the fluorite crystal structure over the temperature range from room temperature to the melting point (which for pure stoichiometric CeO_2 is around 2750 K).[1,10,11] Its structure can be understood as a face centered cubic f.c.c. unit cell of cerium cations with the oxygen anions occupying all the tetrahedral interstitial sites, where each cerium cation is coordinated by eight equivalent nearest-neighbor oxygen anions and each anion is coordinated by four cations.[2,10,12,13]

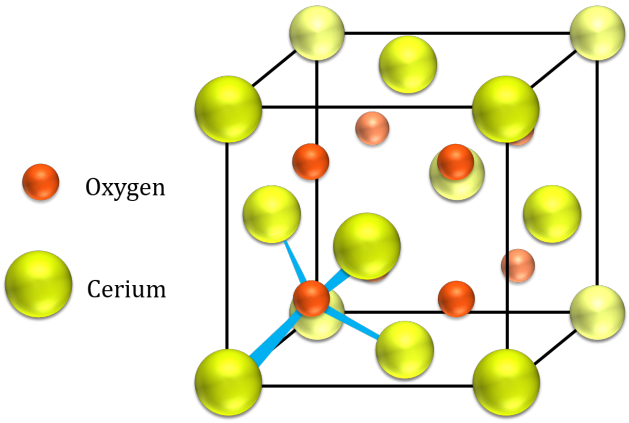

Figure 1.1: Fluorite structure, where the coordination of an oxygen anion is explicitly shown

Cerium in the neutral state has the electronic configuration: [Xe] $4f^1$ $5d^1$ $6s^2$, with the four outermost electrons being valence electrons.[10] Most of the properties of ceria (high oxygen storage capacity, catalytic activity ...) are attributed to the facility of ceria to generate oxygen vacancies and fill them back, which is a direct cause of how easily cerium changes from Ce^{4+} to Ce^{3+}. Partially due to the low potential energy barrier to the electron density distribution existing between the two oxidation states ([Xe] and [Xe] $4f^1$).[14] Although the Ce^{4+} oxidation state is usually considered more stable than Ce^{3+} due to the fact that the electronic structure [Xe] $4f^0$ is a more stable state than [Xe] $4f^1$.[10,15]

Usually it is used the Ce^{3+} fraction to discuss the proportion between the two oxidation states and the concentration of oxygen vacancies present, which is expected to be proportional given that oxygen has in ceria an oxidation state of -2 and thus when leaving, two electrons are accommodated in two adjacent cerium cations. Increasing in this way the proportion of Ce^{3+} ions in order to maintain electroneutrality, as it will be discussed in the following section.[10,16,17]

1.2 Defects

Several types of defects can be found on ceria and they can be classified into intrinsic and extrinsic. The former are caused by thermal disorder (mainly in the form of redox reactions with the surrounding atmosphere) and the later by impurities or introduction of dopants.[10,15] We consider here three thermally generated intrinsic defects, which written in the Kröger and Vink defect notation are expressed as follows:

$$Ce_{Ce} + 2\,O_O \longleftrightarrow V''''_{Ce} + 2\,V^{\bullet\bullet}_O + CeO_2 \qquad \Delta E = 3.53\ eV \quad \text{(a)}$$

$$Ce_{Ce} \longleftrightarrow Ce_i^{\bullet\bullet\bullet\bullet} + V_{Ce}^{\prime\prime\prime\prime} \qquad \Delta E = 11.11\ eV \text{ (b)}$$

$$O_O \longleftrightarrow O_i^{\prime\prime} + V_O^{\bullet\bullet} \qquad \Delta E = 3.2\ eV \text{ (c)}$$

Where O_O and Ce_{Ce} account for oxygen and cerium at their respective lattice sites, $V_O^{\bullet\bullet}$ and $V_{Ce}^{\prime\prime\prime\prime}$ represent an oxygen and a cerium vacancy respectively. $Ce_i^{\bullet\bullet\bullet\bullet}$ and $O_i^{\prime\prime}$ indicate a cerium and an oxygen ion in an interstitial position, where the effective charge (expressed with respect to the usual charge in that same position) is written as a dot for each positive charge and as a prime for each negative one.[10,18]

From the variation in energy it is clear that the most common defect is going to be the formation of oxygen vacancies and oxygen ions in interstitial sites. And normally this defects are present in a low concentration, so no stoichiometric deviation is observed. However, when exposed to reducing atmospheres and/or high temperatures the concentration of vacancies increases and the cation/anion ratio becomes greater than 0.5. This variation in composition is possible due to the localization of the electrons that the oxygen has left behind in the cerium cations, which changes their oxidation state from +4 to +3.[10] The complete process of vacancy formation/elimination may be written as follows:

$$CeO_2 \longleftrightarrow 2\,xCe_{Ce}^{\prime} + (1 - 2\,x)Ce_{Ce} + xV_O^{\prime\prime} + (2 - x)O_O + 0.5\,xO_2$$

This same process can be also expressed in a more simple way like:

$$CeO_2 \longleftrightarrow CeO_{2-x} + x/2\,O_2(g) \qquad \text{with } x < 0.5$$

As a consequence CeO_{2-x} is obtained with x depending on vacancy concentration (with the limit on Ce_2O_3 and thus $x = 0.5$). This cerium oxide of variable stoichiometry is commonly known as ceria.[11] And, according to literature, forms a purely fluorite structure as mentioned earlier for CeO_2 and fluorite-related structures from CeO_2 to $CeO_{1.714}$ (the specific structure will depend on temperature, pressure and oxygen/cerium ratio, although all of them can be regarded as a distortion of the fluorite lattice). For O/Ce ratios lower than 1.714 ceria crystallizes in a body-centered cubic for high temperatures with the limit on dicerium trioxide generally known as sesquioxide Ce_2O_3. Having the CeO_2 flourite structure a lattice constant of a = 5.411 Å, which can vary due to the fact that the radius of Ce^{3+} is larger than that of Ce^{4+}. Thus is dependent on the different proportion of oxidation states for cerium.[10,13]

All this is supported by the fact that several theoretical studies and experiments determined that the predominant defects in ceria are anion vacancies. It is well established nowadays that at low partial pressures of oxygen and high temperatures, some oxygen is released from the ceria due to the creation of oxygen vacancies and as a consequence there is an accumulation of high oxygen deficiency while maintaining

structural integrity (with the limits that have been mentioned). These defects were initially thought to organize in a random way, but in reality this phases could show ordering of oxygen vacancies in a regular fashion. As shown in atomic simulations oxygen vacancy clustering is energetically favourable above a certain threshold value of vacancy concentration.[10,19]

1.3 Size

Another important parameter is the particle size. It was experimentally observed by Tsunekawa et al. that monodispersed ceria nanoparticles (NPs) between 2 and 8 nm show a noticeable increase in their lattice constant compared to that of bulk, measured by XRD.[20,21] The lattice relaxation was a consequence of the reduction in the particles size, with the smallest particles presenting the largest increase in the lattice constant. This was linked to the reduction of the valence of Ce with the decreasing NP size. The change in the charge from +4 to +3 resulted in a decrease in the electrostatic forces that lead to the increase of the lattice constant. This correlation between oxygen vacancies concentration and crystal size was also measured by Zhou et al., founding an increase in vacancies for ceria with crystal size < 10 nm.[22]

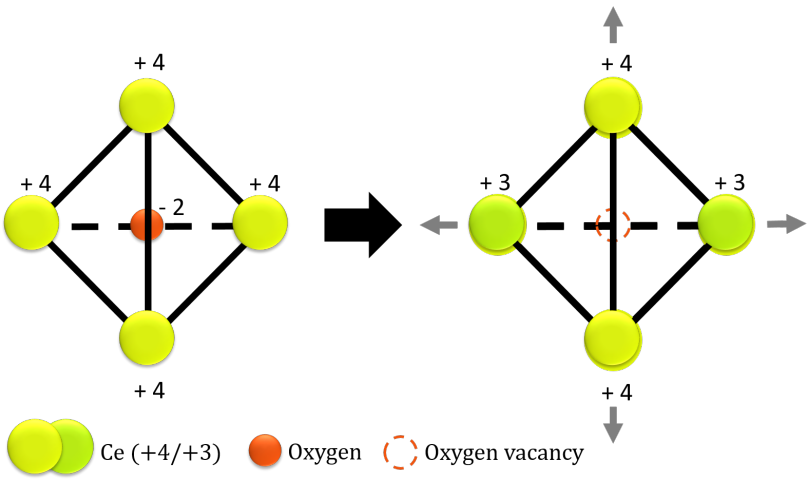

Figure 1.2: Relation between concentration of oxygen vacancies and relaxation of the lattice parameter.[1,12]

Moreover, modelling studies have investigated the ease of vacancy formation in ceria NP with varying size. Neyman et al. investigated the energy of vacancy formation for nanocrystals (NC) $(CeO_2)_n$ with n from 20 to 140. Finding that it was strongly dependent on oxygen position and that was strongly facilitated for dimensions from 2 to 4 nm, reaching a minimum at n = 80.[23]

1.4 Morphology

The shape at the nanometer scale and the facets exposed are factors that can modify significantly the performance as a catalyst. As it has been verified, first theoretically and then experimentally, the exposure of some facets can vary the rate at which oxygen vacancies are created/filled back thus varying the redox activity and performance in the reactions that are driven by the redox behaviour of the catalyst.[24]

For instance, theoretical studies were made through atomistic simulation in order to gain insight into the bulk and surface properties of ceria. By means of empirical models of interatomic potentials adjusted using experimental data or ab initio methods. The later consists of applying the principles of quantum mechanics to solve the many-body problem, which means solving numerically the different reformulations and approximations of the Schrodinger equation for our system. One of the first conceived and simpler approaches is Hartree-Fock, which considers the solution of an electron interacting with an average charge density of all the other electrons (Mean-Field approach) and an antisymmetric ansatz called the Slater determinant (a requirement related with the indistinguishability of electrons). Using Hartree-Fock some groups studied the stability of the different facets and determined their surface energy.[25] Another popular approach is Density Functional Theory (DFT), which solves the Kohn-Sham equations to find the charge density by means of pseudopotentials. Using DFT Nolan et al. calculated the low index surface Gibbs free energies and their results where in agreement with the ones found using Hartree-Fock by other groups (shown below in Table 1.1). The stability of these surfaces has to do with the number of coordinative unsaturated sites, surface polarity and defects. These studies also covered the calculation of the vacancy formation energy on each of the three low indexed surface, finding that the most stable surface had the highest vacancy formation energy.[26]

Here the Miller indices are introduced as a notation to describe the different planes the ions can form in a crystal. Being a, b and c the three lattice vectors that define the unit cell, the vector $n = ha + kb + lc$ would be the normal vector to that family of planes. Where h k and l can be seen as the number of times the planes intersect a, b and c respectively. And thus when the facet or plane hkl is mentioned, we will be referring to the corresponding Miller indices of that plane.

The thermodynamically most stable crystallographic facet was found to be the 111 followed by the 110 and the least stable being the 100. Followed by the 211, unfortunately it rapidly reconstructs into a stepped 111 surface. Experimentally and theoretically surface relaxation (the displacement of surface ions to decrease the energy of the surface) has been measured and calculated with DFT. Finding little relaxation in the 111 surface and greater one for 110 and 100. Other higher indexed surfaces are even more unstable thereby more unlikely in real systems. The majority of the studies have focused in the three more stable and common facets of ceria, the ones with the lowest index.[19,24,27–29]

Table 1.1: Coordination number: number of atoms bonded to each ion at the surface, Unsaturated sites: potential sites at which an adsorbate can bond at the surface. Surface energy: energy required to form each surface. Vacancy formation energy: energy necessary to create an oxygen vacancy. Table reproduced from[24]

	111	**110**	**100**
Coordination number	O (3), Ce (7)	O (3), Ce (6)	O (2), Ce (6)
Coordinative unsaturated sites	O (1), Ce (1)	O (1), Ce (2)	O (2), Ce (2)
Surface energy (eV)	0.69	1.26	2.05
Oxygen vacancy formation energy (eV)	2.60	1.99	2.27

It should be noted that the error in DFT calculations is systematic, and thus the interesting data is the energy differences and not the absolute values. These variations come from the fact that each facet presents a different arrangement of cerium and oxygen even though they are all coming from the same fluorite structure. The 111 for example is terminated in oxygen (which has been measured experimentally[19]) with a repeating O−Ce−O−O−Ce layer structure. Due to the difference in electronegativity between Ce and O, the charge density of the valence electrons migth be displaced with respect to their nuclei leading to what is known as polar bonds. In this case, as we have one oxygen layer at each side of the cerium surface the dipole moments cancel out. So it has no net dipole moment due to the repeating layers of O-Ce-O which ensures charge neutrality. And it has only one coordinative unsaturated site for each ion. Using VESTA[30] we can visualize the different facets (in blue) in the fluorite structure of ceria, being the 111 depicted in Figure 1.3.

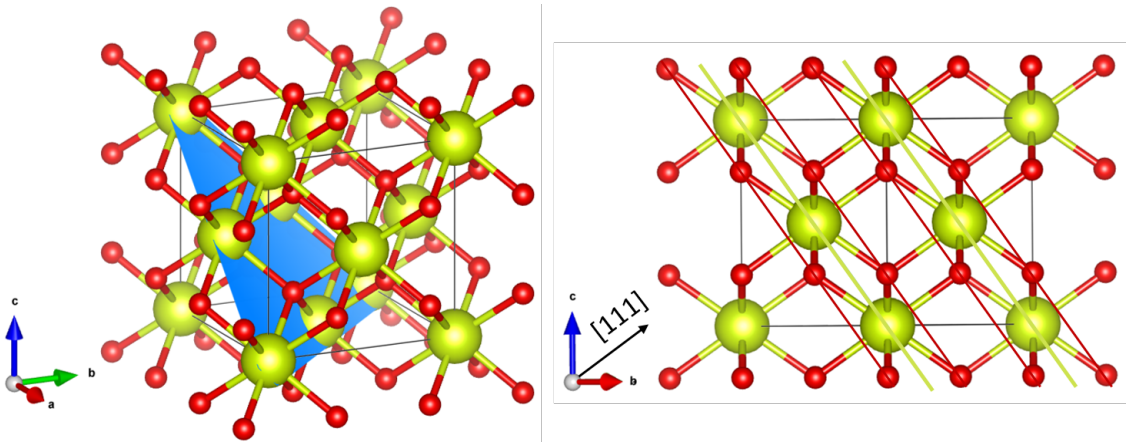

Figure 1.3: Plane 111 seen from two different angles. Oxygen in red and Cerium in yellow

Conversely, the 110 has both oxygen and cerium in each plane being both of them present on the surface in stoichiometric proportion (which was also measured experimentally[19]). And thus each layer has zero net charge. Studies have shown that the surface relaxation in this facet traduces in both ions moving inwards but the cerium cation moving further than the oxygen anions. With the oxygen ions shifting towards the nearest cerium ion in the same layer to compensate for the asymmetric inwards vertical relaxation.[19] In this case, anions have one unsaturated coordinative site at the surface while cations have two.

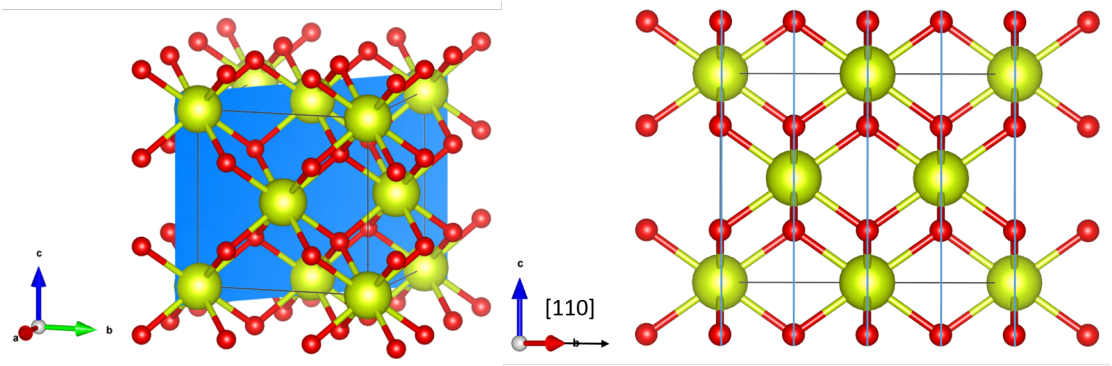

Figure 1.4: Plane 110 seen from two different angles

The most unstable of the three low index surfaces is the 100, consisting of O-Ce-O-Ce repeating layers, which generates a dipole moment perpendicular to the surface due to the sequence of charged (cation-anion) planes. And therefore requires a reconstruction since dipolar surfaces are unstable. Usually this reconstruction consists on the removal of 50% of the terminating species. Which are considered to be oxygen, due to the lower surface energy in that case. If we remove 50% of surface oxygen then we obtain two coordinative unsaturated sites at the surface for each ion. The 100 surface undergoes the strongest relaxation with the terminating oxygen anions shifting inwards and a reduction of 7.6 % in the last Ce-O bond distance between surfaces.[19] Which could account partially for the higher vacancy formation energy on this facet even though is the facet with lowest coordination value for oxygen.

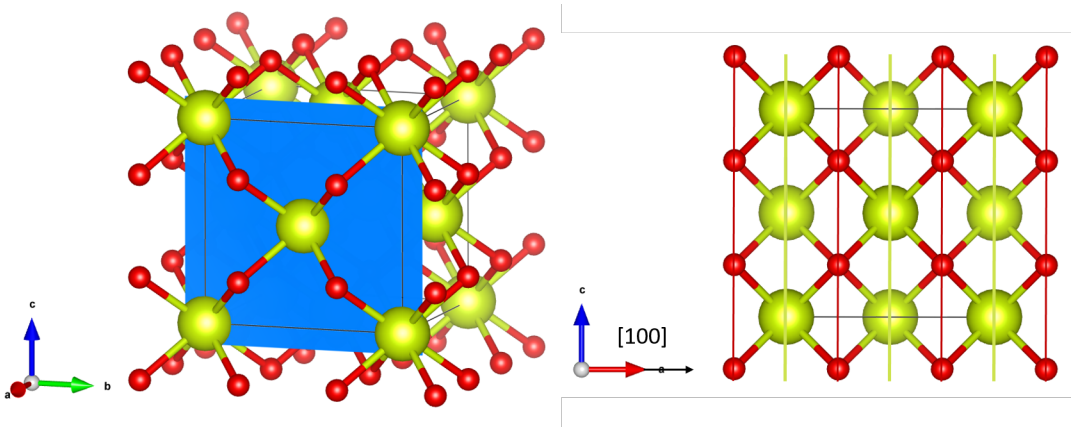

Figure 1.5: Plane 100 seen from two different angles

The different facets show different reduction properties, which were firstly discovered by theoretical simulation studies which are a major part when it comes to understanding the catalytic properties of ceria. This studies yield different oxygen vacancy formation energy for each facet. This vacancies can act as oxygen activation centers in oxidation reactions and thus are strongly related with catalytic activity. Looking at the vacancy formation energies of each configuration yielded by DFT calculations we can conclude that the order of reactivity for the vacancy formation (and thus catalytic activity whenever vacancy formation is the limiting step) is: 110 $>$ 100 $>$ 111. This statement set the basis for several experimental studies on ceria NC.[12,24,27,31]

1.5 Synthesis techniques

A clear correlation between crystal shape and catalytic activity/selectivity was established.[2,24,32] By synthesizing, characterizing and testing in prove reactions different ceria-based materials which had distinct morphologies at the nanometer scale, and thus exposed different facets of the crystal.

In a typical synthesis two stages can be distinguished: nucleation and growth. Nucleation is the first part of any crystallization process. When the concentration of the different components (ions, molecules or atoms) becomes high enough and they start aggregating forming nuclei. In the second part these nuclei serve as seeds for further growth to form larger structures. The morphology of which will be controlled by an interplay between thermodynamics and kinetics. Under thermodynamic control the greatest proportion of the most stable surfaces will be formed. According to the Gibbs-Wulff theorem, the equilibrium morphology of a NC is the one that minimizes surface energy for a given volume. In the case of ceria would be a polyhedron shape enclosed by 111 facets. And thus if a crystal of higher surface energy is required, its synthesis will necessarily take place through the kinetic control of nucleation and growth rate of the crystal in the different directions, by reaching a metaestable NC shape tunning the reaction conditions and stopping the growth before the reaction reaches equilibrium.[24,27,28,33,34]

The growth rate of the material in the different directions can be changed by means of modifications in surface anisotropy using additives or changes in experimental conditions such as pH, temperature, nature of the precursors... Resulting in several types of structures depending on the relation between the growing rates in each direction. 0 D structures such as nanospheres, nanocubes, and nanopolyhedra are the result of maintaining the same growth rate in each direction. 1 D structures like nanowires, nanorods and nanobelts are formed increasing significantly the growth rate in one specific direction. While 2D nanomaterials are the result of the important reduction in the growth rate of a specific direction, thus creating flattened nanoplates and nanosheets. Even hollow or tubular structures can be made. Although ceria NP usually crystallize in polyhedral shapes enclosed mainly by low energy surfaces, mainly 111 but also 110 and 100.[27,28,32,33,35–38]

Inorganic/organic additives are used as capping agents due to their selective

binding properties onto the different facets, thus blocking the growth of the crystal in the desired direction for a specific concentration of the surfactant. Whenever capping agents are used it appears the necessity of removing them effectively after the growth of the crystal, being then a disadvantage when CeO_2 with maximum reactive sites is required.[10,36] In this cases a good alternative is the employment of a hydrothermal/solvothermal process (although a combination of both techniques is also possible as we will see), which is one of the most simple and efficient ways to synthesize ceria NC with shape control and without the necessity of surfactants or templates.[27,38,39] With this method, a cerium salt ($Ce(NO_3)_3{\cdot}nH_2O$ or $CeCl_3{\cdot}nH_2O$ for example) is dissolved in water and mixed with a base (NaOH, KOH or NH3 among others) obtaining a suspension that is transferred into a Teflon-lined autoclave performing a thermal treatment between 373-493 K for 8-50 h. The structural isotropic nature makes it difficult for ceria to grow anisotropically to produce other shapes than polyhedral crystals. However, the intermediates in the reaction during the hydrothermal/solvothermal process or the counterions of precursors can function as capping reagents, blocking in this way the growth in some specific directions and forming nanoshapes.[10,27,31,40,41]

Using these techniques among others, researchers were able to prepare rods, cubes, wires, tubes, spheres... and to relate their catalytic performance to the proportion of the different facets that were exposed by each morphology. Experimentally nanorods were found more active than nanoparticles (NP) in various catalytic reactions and the difference was attributed to the higher proportion of 100/110 facets with respect to the mainly 111 facet exposed in polycrystalline particles, thus establishing a correlation between the facets and catalytic activity which at its turn related with oxygen vacancy formation rate.[1,2,24,37,41,42]

1.6 Reaction mechanism

Among the different applications in which ceria can be used as a catalyst, one of the most relevant is CO oxidation to CO_2. Ceria as a catalyst is important to eliminate toxic exhaust gases from combustion (in cars, power plants...) and for its use as electrolyte material in Solid Oxide Fuel Cells (SOFC) and Proton-exchange membrane fuel cells (PEMFC). In the former, the oxidation of CO is conducted to prevent the poisonous CO from escaping to the atmosphere as it binds to hemoglobin and represents a public health issue. In the later, ceria has potential as solid oxide ion conducting electrolyte membrane between cathode and anode in SOFC. It would lower the temperature operation of SOFC and PEMFC due to its superior ion conducivity (which is related with the oxygen vacancies in the lattice) and eliminate CO which is detrimental for the efficiency of PEMFC.

In CO oxidation catalyzed with ceria we have to consider the chemical dynamics at the gas-surface interface for instance. The species in gas form may exchange translational and internal energy with the surface and some of them will lack the momentum to escape the gas-surface potential well and thus become trapped. This molecules may react with other adsorbates as it is the case in CO oxidation and in

time acquire sufficient thermal energy to desorb into the gas phase.[43]

CO oxidation on ceria catalysts is known to follow under stationary conditions the Mars-van Krevelen reaction mechanism. The characteristic feature of the reactions that follow this mechanism is that some products leave the catalyst surface with at least one of the constituents of its lattice. In this case adsorbed CO leaves the surface after being oxidized by adsorbed O. The rate of oxidation of adsorbed CO depends on the number of available active sites, the oxygen diffusion rate in the ceria lattice as well as the adsorbed oxygen replenishment rate from bulk ceria and gas-phase oxygen among other things.[29] As it is shown in the following scheme:

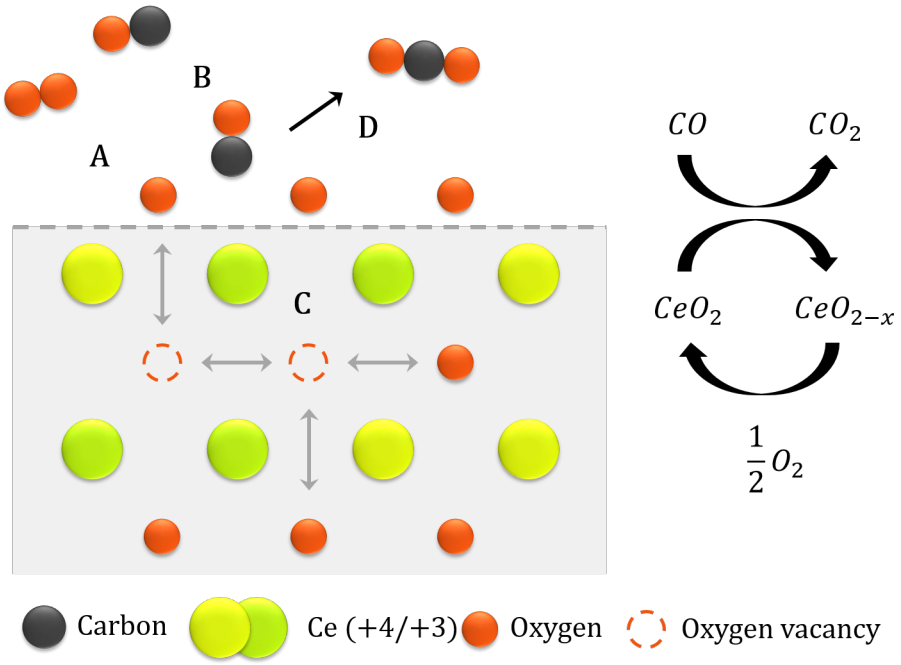

Figure 1.6: Scheme of the Mars-van Krevelen mechanism for CO oxidation on ceria.[2] In the case where the exposed facet is the 100.

During the process, CO extracts an oxygen atom from the surface creating an oxygen vacancy. O_2 is then adsorbed onto the surface and dissociates, filling back that vacancy (see Figure 1.6 A). This adsorbed oxygen is in the form of superoxides (O^{2-}) or peroxide (O^{-}). Both are intermediates in the process of oxygen gas incorporation into the lattice. Ce^{3+} ions (oxygen vacancies at the surface) can serve as coordination sites to induce the formation of these active oxygen species (adsorption and dissociation of oxygen gas).[13,44,45] These species react with adsorbed CO (B) to give CO_2 and finally abandon the surface after its desorption (D).

Diffusion of oxygen anions as well as other transport properties are determined by the concentration and mobility of vacancies (C). This properties play a key role in the applications mentioned before: solid oxide electrolytes and in catalysis, because the material has to be reduced rapidly by the reagent and reoxidized by means of the incorporation of gaseous oxygen into the lattice. Whenever the availability of oxygen from the gas phase is not constant or the creation of oxygen vacancies at the surface is not a limiting step, oxygen diffusion from the bulk to the surface becomes

relevant and starts to play a role. And thus ceria can supply oxygen when there is oxygen gas deficit or reserve it in the case of abundance.[44]

1.7 Metallic NP supported over ceria

Ceria can be used as active support in many reactions. The deposition of active components enhances the creation of oxygen vacancies and thus oxygen mobility by means of promoting the cerium ion reduction at lower temperatures as shown by Temperature Programmed reduction (TPR) profiles in some studies before and after metal NP deposition.[46] Oxygen vacancies also strengthen the interaction between the active material and the support which is indispensable to stabilize the metal NP on the support.[46,47] Both properties can form a synergistic effect and improve the performance of CeO_2-supported catalysts.[48]

For instance, the low-temperature oxidation of CO can be catalyzed by highly dispersed Au NP supported on CeO_2 and its activity is controlled by several factors such as the ability of the support to provide oxygen for the reaction (which will depend on the facets exposed and thus morphology), the size and morphology of the metal NP, the oxidation state of gold atoms...[46,49] Moreover, a remarkable increase in selectivity in the CO preferential oxidation (COPROX) reaction has been reported as well,[50] which is the oxidation of carbon monoxide in the presence of hydrogen, an important reaction when it comes to the applications of ceria in PEMFC.

To explain the mechanisms of this synergy it has been proposed that ceria supplies reactive oxygen in the form of superoxide and peroxide species to the gold NPs (see Figure 1.7 A) while CO is adsorbed on them[47] (B). Through an electron transfer from the gold atoms to the support, the concentration of Ce^{3+} is influenced by the deposited metal, which can be seen as the support influencing the valence state of the metal element. In this sense, the metallic NP accelerates the adsorption of gaseous O_2 and the migration of bulk oxygen to the surface (C) through the creation of oxygen vacancies at the surface.[48,51] Due to that the active sites are considered to be formed by the perimeter of the contact area between Au and the cerium oxide support for low temperature CO oxidation (D).[46,47,49] As the active oxygen species are supplied by the ceria surface and adsorbed CO by the metallic NPs. This is supported by the fact that an increase in surface content of Ce^{3+} (and thus oxygen vacancies) is observed after the addition of NPs onto ceria.[46]

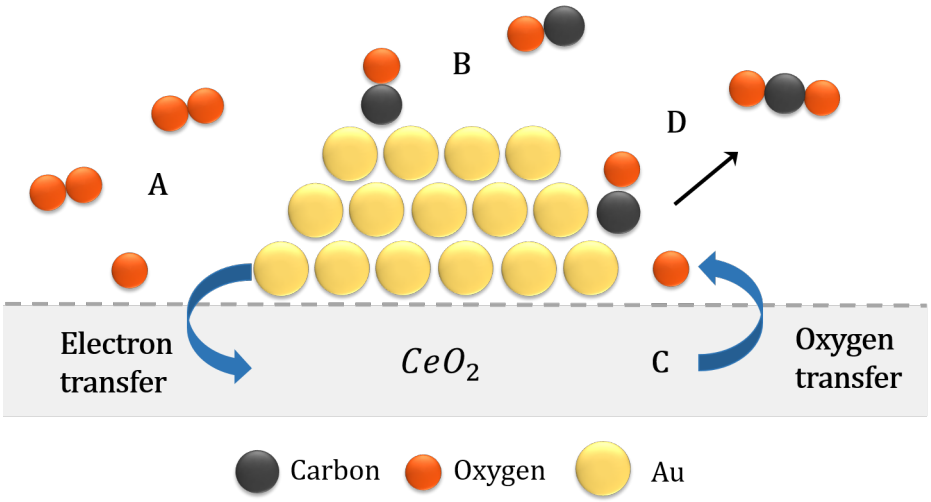

Figure 1.7: Scheme of the Mars-van Krevelen mechanism for CO oxidation on ceria with Au NP.

Taking these ideas into account, a structure was proposed for this strongly bound metallic nanoparticles by Liu et al.[47] The faceted Au NP is divided in four different domains, each of them with a unique function. The internal gold atoms can be regarded as supporting blocks as they do not participate directly in the reaction. The surface and sub-surface layers are responsible for the adsorption of CO molecules. The atoms at the Au-ceria interface perimeter are viewed as the active sites for the reaction between oxygen species and adsorbed CO molecules to form CO_2. And the gold atoms at the interface between the NP and the support away from the perimeter are responsible for the strong anchor of the metallic NP. It is generally accepted that small particle size (<5 nm) is indispensable for a high catalytic activity,[46,47,52] which was investigated by Valden et al. by establishing a correlation between specific activity of the metal and their band gap (that varied with NP size). Concluding that CO oxidation turnover frequencies (TOF) were higher for NP between 2.5 and 3.5 nm and associating the size sensitivity to quantum size effects.[53]

In accordance with these affirmations a correlation is often established between the presence of ionic Au (Au^{+3}) together with a good Au dispersion and catalytic activity for CO oxidation. As Au dispersion and strong interaction with the support can lead to a higher reducibility of ceria.[46,49,50,52,54] As well as preventing sintering which occurs when weak interactions between the support and the NP break uppon an increase in temperature. Simultaneously, the electronic states and the stabilization of finely dispersed Au depend on the facet exposed by the support (through oxygen vacancy creation, the easier the creation of oxygen vacancies the easier the Au NP stabilization and the stronger the interaction). So in nanorods for example, where the energy of oxygen vacancy formation is lower, Au NP will be better stabilized and dispersed and the fraction of Au^{+3} will be higher.[50]

In short, gold nanoparticles are known to adsorb CO but they do not strongly adsorb and activate oxygen molecules which is the role of the reducible oxide support for our case. Because of that, combining Au with a second metal able to dissociate oxygen we would improve the catalytic activity.[55] In fact, the use of bimetallic

nanoparticles in catalysis has been investigated over the past two decades, with the objective of exploiting synergistic effects between metals due to electronic or structural modifications of the active sites[56] to achieve enhanced catalytic properties. Among the most common combinations is Au with a secondary metal, which has promising results for CO oxidation. The secondary metal is much more susceptible to oxidation than gold as the latter has the highest electronegativity in the transition metals (2.54 eV). In a reactive atmosphere, phase segregation tends to take place, with the secondary oxidized metal forming patches or shells around the gold-rich core. Thereby acting as a promoter of oxygen species during the reaction and also preventing sintering at high temperatures.[57] This anti-sintering behaviour is often described as the segregation of the second metal on the surface of Au NP during calcination resulting in the formation of oxides which prevent the NP from aggregation.[58] Au−Cu nanoparticles for example have been investigated in other supports than ceria with outstanding results for low-temperature CO oxidation.[57]

It has been reported by Guardia et al. that for the case of AuCu bimetallic nanoparticles supported on Al_2O_3, copper was active only in the form of CuO as a layer or patches around the mainly Au NP and inactive in the metallic, alloyed with Au state. The catalyst was deactivated when it was oxidized at 350 °C due to a segregation of the CuO species from the Au NP (in other words a weak interaction between them) and activated when put under reaction conditions,[56] when the CuO species migrated back to the Au NP. Which was in agreement with other studies that reported that the interface between Au and CuO is the key for the catalyst activation. Mozer et al. showed that while low Cu content was beneficial for the oxidation of CO, high copper concentrations caused the blocking of Au active sites.[59] This is in accordance with other studies like the one conducted by Sandoval et al. in which the activation of Au−Cu/TiO_2 was attributed to the formation of an Au/CuO/TiO_2 structure.[55]

Chapter 2

Objectives

The main purpose of this thesis is to understand the different catalytic properties of different ceria-based materials and to ascribe the different behaviours to structural, morphological and synthesis variations among other factors to find the path to follow in the design of future catalyst with enhanced properties. To achieve that, the following specific objectives will be pursued:

- Synthesize different ceria samples using procedures found in the literature.
- Test those samples in CO oxidation and characterize them using XRD, SEM and XPS.
- Decorate the samples with equal loading of preformed AuCu bimetallic NPs.
- Test the decorated samples in CO oxidation and characterize them before and after the reaction.
- Explain the results using the available literature and the theoretical background as well as the results from the characterization studies. Outline the relations between different structures and compositions to catalytic properties. Make a suggestion on the future steps that could be taken in the design of an enhanced catalyst.

The use of homogeneous preformed bimetallic NPs will allow us to assign the different catalytic performances to the NP-support interaction and the properties of the latter. Excluding in this way changes in the size, morphology or loading of the bimetallic NPs. Although in practice commercial catalyst are non-uniform, it is convenient in our case to control with precision any possible source of variability. In order to devise a reliable explanation for the different levels of catalytic activity.

Chapter 3

Pure ceria as catalyst

3.1 Experimental: synthesis and catalytic test

Three different synthesis were conducted to achieve ceria with different catalytic activities. The first sample (S1) was produced using 4.882 g of $Ce(NO_3)_3{\cdot}6\,H_2O$ and 1.366 g of hexadecyltrimethylammonium bromide (CTAB) to obtain a 1:3 molar proportion (CTAB : Ce^{3+}), mixed using magnetic stirring and ultrasonication in 135 ml of deionized water until the precursors were completely dissolved. Afterwards, 15 ml of $NH_3{\cdot}H_2O$ 28 % were added with a buret drop by drop. A change of color was observed as the solution acquired a brownish tone with the apparition of a clear precipitate. The mixture was then poured into a 300 ml capacity Teflon-lined stainless steel autoclave, closed and maintained at 433 K during 24 h. After that, a whitish precipitate was obtained, which was carefully washed repeated times with deionized water. Ultrasonication was used in order to disperse correctly the nanoparticles and a centrifuge to separate the solution with ammonia and CTAB from the nanoparticles, until all the additive was removed and the pH restored to neutral. Finally, to remove the water two more washes were carried out using ethanol before introducing the clean precipitate into an oven at 353 K and letting it dry overnight. The dried precipitate was pulverized using a mortar and a pestle until it appeared homogeneous and fine.

The second sample (S2) was produced with a similar method changing the conditions and concentration of additive. 4.882 g of $Ce(NO_3)_3{\cdot}6\,H_2O$ were mixed with 2.7335 g of CTAB to achieve a molar proportion of 2:3 (CTAB:Ce^{3+}). Under magnetic stirring and ultrasonication using 135 ml of distilled water. Subsequently, 15 ml of $NH_3{\cdot}H_2O$ at 28 % w/w were added using the same procedure as in S1, being able to observe once more the change in color and the precipitation of cerium hydroxide. The mixture was then introduced in the same 300 ml Teflon-lined stainless steel and maintained at 373 K for 8 h. After that the whitish precipitate was washed several times with deionized water and ethanol before introducing it to an oven at 353 K overnight. The final step was once again the pulverization of the sample using a the mortar and pestle.

The third and last sample (S3) was produced dissolving 2 mmol of $Ce(NO_3)_3{\cdot}6\,H_2O$ (0.86846 g) in 80 ml of deionized water. Followed by the addition with a Pasteur pipette of 2 ml of $NH_3{\cdot}H_2O$ at 28 % w/w. This time a 100 ml Teflon-lined stainless steel autoclave was used and put into an oven which was maintained at 493 K for 24 h. After that the precipitate was washed with water and ethanol several times and dried at room temperature during 48 h. The pulverization was carried out as usual.

Also two more samples were considered, nanorods (R) and polycrystals (P), which were already synthesized and available at the time. To put it briefly, both of them were produced using a electrospray to add an aqueous solution of 0.4 M $Ce(NO_3)_3{\cdot}6\,H_2O$ to another aqueous solution with a concentration of (0.2 / 9.0) M NaOH (P/R) under stirring for 30 min. Subsequently transferred to a PTFE-lined cylinder and sealed in a stainless steel autoclave and heated at (423 K / 373 K) (P/R) for 24 h. After that, the samples were washed with water and ethanol and dried at 333 K overnight.[42] According to the same article the sample P polycrystals measured between 5-15 nm and were round-shaped. As for the rods sample, it was determined a diameter between 10-15 nm and approximately 0.2-0.5 µm in length.[42]

The synthesized samples were characterized using a Scanning Electron Microscopy (SEM) at 5 kV using a Zeiss Neon40 Crossbeam Station instrument equipped with a field emission source. For R and P images of previous articles were used.[42] X Ray Diffraction (XRD) was carried out for four of the five samples (with the exception of S3 as there wasn't enough sample to produce the XRD pattern adequately) using a Bruker D8 diffractometer with Cu Kα radiation (40 mA, 40 kV). And at last but not least, calculating the approximate size of the crystal domains using the Scherrer equation.

$$\tau = \frac{K\lambda}{\beta cos\theta_m} \tag{3.1}$$

Were τ is the mean size of the crystalline domain, which will be smaller or equal to the grain size depending on whether the sample is polycrystalline or monocrystalline. K is a dimensionless shape factor with a typical value of 0.9, λ the X-Ray wavelength, β is the full width at half maximum (FWHM) in radians and θ_m is the angle corresponding to the maximum. In other words, the angle which satisfies the Bragg equation for the corresponding plane.

In order to find accurately β (FWHM) of the first peak (corresponding to [111]) for each sample a Gaussian function was adjusted:

$$G(\theta) = \frac{A}{\beta}\sqrt{\frac{\ln 2}{\pi}}e^{-\ln 2\left(\frac{\theta-\theta_m}{\beta}\right)^2} + a\theta + b \tag{3.2}$$

Where A is a constant which takes into account the area of the peak to avoid being limited to the normalized Gaussian function, β is the FWHM we are looking for, θ_m is the angle corresponding to the maximum and a and b two constants which take into account the background noise.

Moreover, using Bragg's Law and the relation between the Miller indexes and the distance between planes for a cubic system is possible to calculate the lattice parameter for each sample.

$$2d_{hkl}sin\theta_m = \lambda \qquad d_{hkl} = \frac{a}{\sqrt{h^2+k^2+l^2}} \tag{3.3}$$

Where d_{hkl} is the distance between the planes with Miller indices hkl, λ the wavelength of the X-Rays used (which for our case is 1.54 Å), a the lattice parameter and θ_m the angle at which diffraction is observed. Combining both equations we obtain:

$$a = \frac{\lambda}{2sin\theta}\sqrt{h^2+k^2+l^2} \tag{3.4}$$

The first catalytic test was the CO oxidation reaction. The main set up of the experiment is described in Figure 3.1 . The tubes, the plug flow reactor (PFR) reactor and connections were purchased from Swagelok and the reactor was put into a vertical oven to prevent the formation of preferential channels due to gravity (In a horizontal reactor a gradient in pressure perpendicular to the flow direction creates the apparition of gas preferential channels in the catalyst, that are used by the gas mixture instead of obtaining a homogeneous flow through the sample). The gas stream was measured at the beginning of each experiment with a soap-bubble-meter. A gas chromatograph (Micro GC Agilent 3000A) equipped with MS 5A, Plot U and Stabilwax capillary columns and TCD detectors was used to measure on-line gas concentrations every 4 min. Which was calibrated by sending known and constant fluxes of the relevant gases into the GC and relating the area of the signal given by the TCD (Thermal Conductivity Detectors) for each one with the total amount of each gas. For each test 2 mln/min (ml at normal conditions of temperature and pressure) were used of CO and O_2 as well as 96 mln/min of N_2 as a carrier gas obtaining a total constant flux of 100 mln/min. The temperature of the reactor was changed using a PDI controller located in the oven surrounding the reactor, in steps of 20 degrees from ambient temperature up to 100 % of conversion of CO to CO_2. For each temperature the corresponding transient time was waited until the reaction stabilized. The main criteria to decide whether equilibrium was reached was the reduction of the variation of the concentration of CO_2 between injections to the noise level of the instrument.

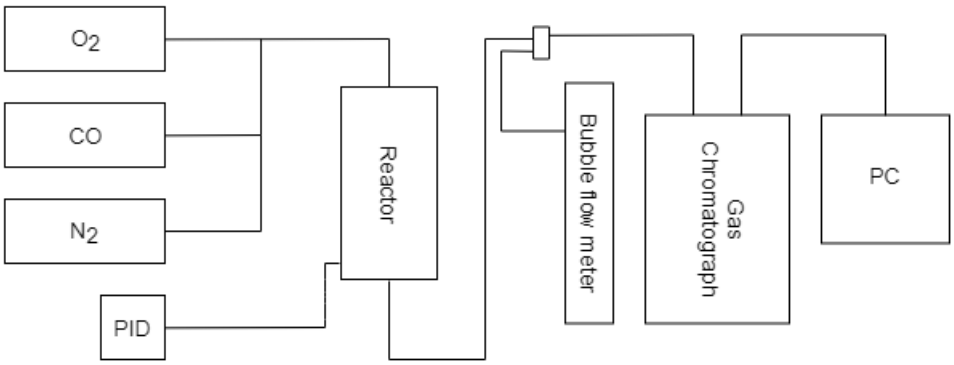

Figure 3.1: Scheme of the experiment setup

For each catalyst the same experiment was carried out and 100 mg of sample were carefully measured and introduced into a falcon tube. This was followed by the addition of Silicon Carbide. A material used in heterogeneous catalysis for its resistance to oxidation and thus inert character in redox reactions. The support helped to control the volume occupied by the catalyst in the reactor regardless of the density of the morphology. Which was important to attribute the differences in activity between samples to other factors than the residence time in the reactor. The volume of the mixture of Silicon Carbide and cerium oxide was maintained constant in all the experiments at 2.6 cm^3. This yielded a gas hourly space velocity (GHSV) of 2300 h^{-1}. The sample was introduced into the vertical reactor and sealed in both sides with wollen glass to prevent the solid from escaping while letting the flow of gas into and out of the reactor.

The quantities of each gas were registered and processed afterwards for each sample. The CO conversion and CO_2 evolution as a function of temperature and CO_2 as a function of time were obtained. Where the CO conversion was calculated using for low values of CO_2:

$$CO_{conversion} = \frac{CO_2}{CO_{in}} 100 \tag{3.5}$$

And for higher values of CO2 the conversion was calculated as:

$$CO_{conversion} = \frac{(CO_{in} - CO_{out})}{CO_{in}} 100 \tag{3.6}$$

This is due to the fact that for low temperatures, when the reaction is slow, the oscillations in the value of CO_{out} due to the GC noise were greater than the CO_2 produced and thus equation 3.5 yield unrealistic values of CO conversion. The change from one formula to another is ideally done when both of them give similar results and they are treated as equivalent due to the stoichiometric relation between the two species in the reaction (for each mol of CO_2 produced we should have 1 mol

of CO less). With respect to the CO_2 evolution, the gas cromatograph is calibrated to give mln/min. So to convert this into the molar flux we only have to apply the ideal gas equation PV=nRT taking into account the pressure is constant and equal to one atmosphere as the circuit is open and the temperature at the end of the circuit is the ambient one. Thus the relation between moles and volume is given by:

$$V\frac{P}{RT} = V\frac{1\ atm}{0.08205746\ \frac{L\ atm}{mol\ K}\ 298\ K} = \frac{V}{24.45312} = n \tag{3.7}$$

The evolution of CO_2 against temperature is normalized due to the fact that the experiments were carried out in different days and due to some minor leaks and errors the total maximum flow of CO_2 was not constant from one sample to another. So the relevant information would be the normalized evolution of CO_2 or the conversion of CO as they don't depend on absolute values.

3.2 Results: characterization and test

With the XRD pattern we confirmed the face centered cubic (fcc) crystallinity of the samples by comparing to known data and assigning each peak to the corresponding family of planes taking into account the systematic absences for the fcc system (In some systems the destructive interference caused by the simultaneous diffraction of X-Rays in two different families of planes yield no intensity in the XRD pattern, which is shown in Figure 3.2).

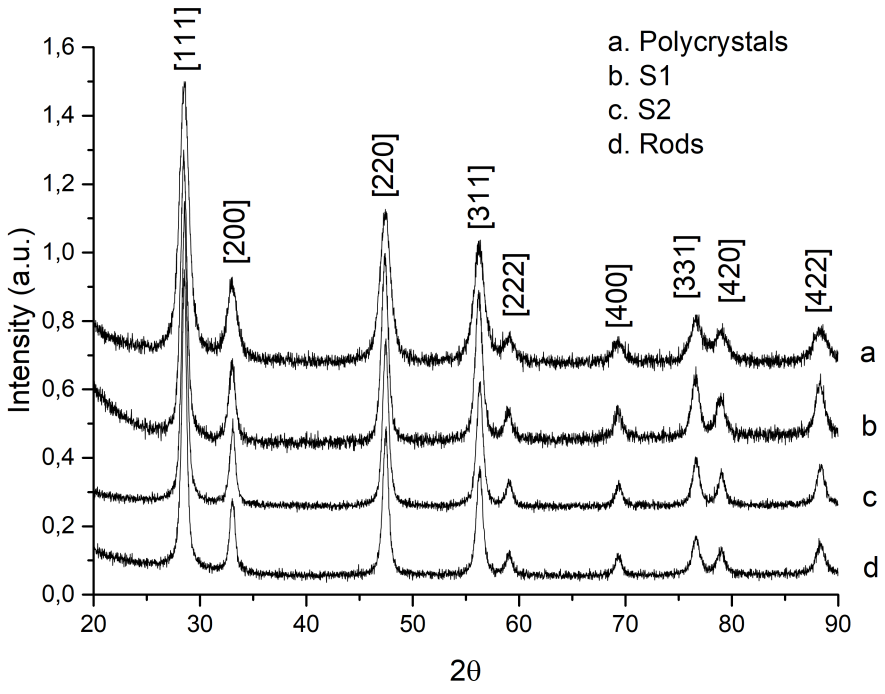

Figure 3.2: XRD pattern of the samples.

The values of the crystalline domains found after adjusting the Gaussian function (equation 3.2) and applying the Scherrer formula (equation 3.1) are listed in Table 3.1. The lattice parameters calculated from equation 3.4 and the sizes of the NPs from the histograms of the SEM images are also included.

Table 3.1: Crystal domains calculated from the Scherrer equation taking $K = 0.9$, lattice parameters amd results from the histograms of the SEM images for each sample.

	Crystal domain (nm)	**Lattice parameter (Å)**	**Nanoparticle diameter (nm)**
S1	22.2	5.427	22.6
S2	26.4	5.416	25.4
S3	-	-	26.3
Rods	29.4	5.419	-
Polycrystals	16.5	5.419	5-15[42]

With the SEM images it was possible to make an educated guess on the morphology. Which turned out to be polycrystals for S1, S2 and S3. Using the Fiji Image J free software, an histogram of the different samples was made with at least 300 nanoparticles for each sample (Figure 3.3). And the results clearly pointed out that the S1 sample was slightly smaller than the other two with an expected size of 22.56 nm while the other two had a mean diameter of 25.37 nm (S2) and 26.28 nm (S3). Comparing the values obtained from the XRD pattern with this ones we can assume the three samples are monocrystalline (Even though we refer to the morphology of the samples as "polycrystals" due to the non-exclusive presentation of different facets, the samples only have one crystal domain and thus are monocrystalline). The differences between the two methods can be attributed to experimental error and the shape factor K which depends on the geometry.

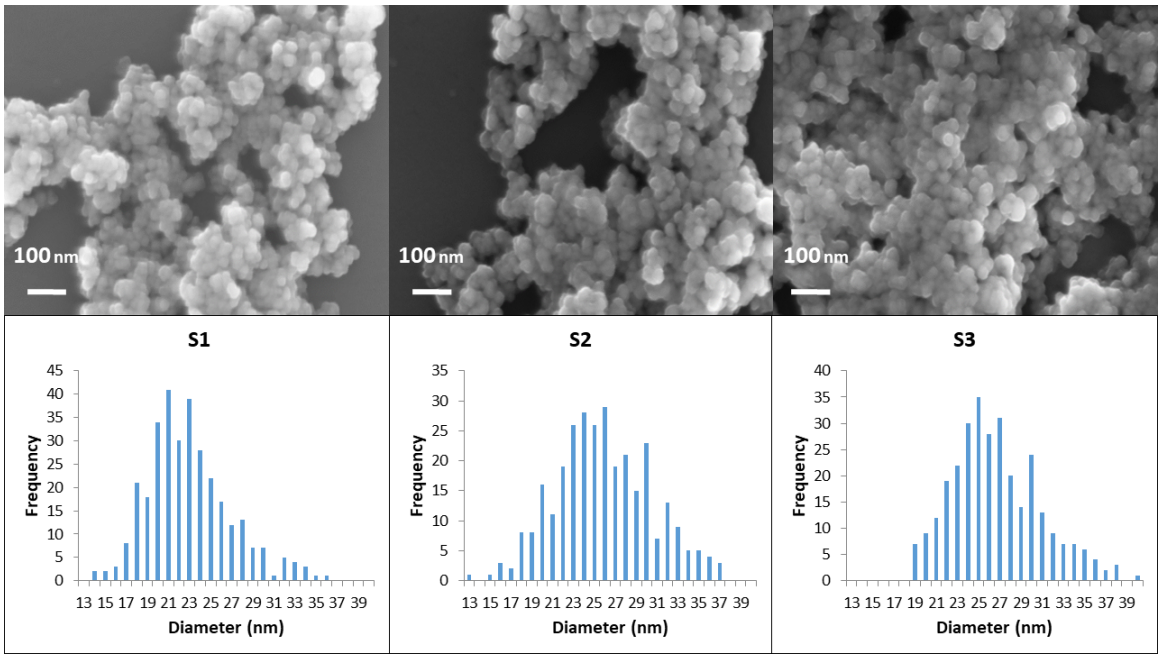

Figure 3.3: SEM images and Histograms

SEM images of the preformed rods and polycrystals are included in Figure 3.4 for completeness, taken from.[42]

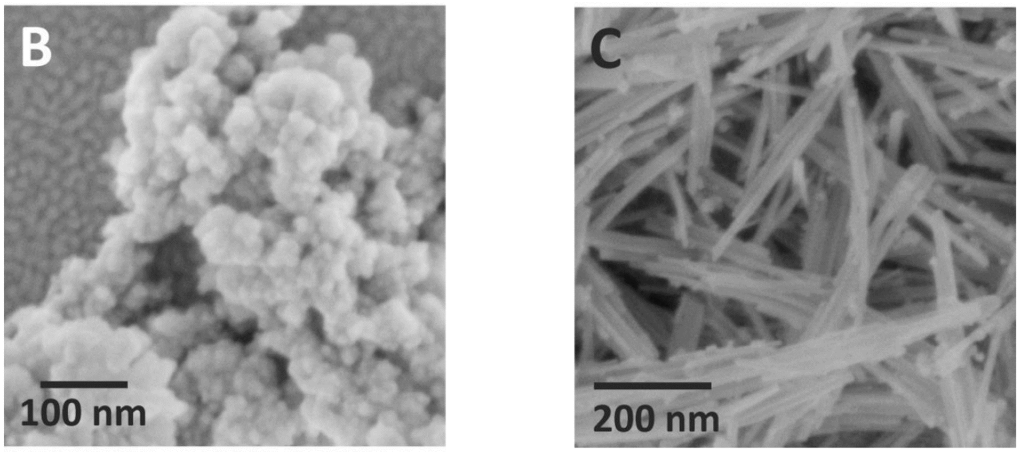

Figure 3.4: SEM images of CeO_2-nanopolycrystals and CeO_2-nanorods[42]

The results of the catalytic test indicate that, even though they have the same morphology and similar size, there are differences between the samples S1, S2 and S3 which endow them with differences in catalytic activity. With the highest CO conversion for S1 and the lowest for S3, being S2 similar to S3 at low temperatures and similar to S1 at higher ones. Little difference is observed between S2 and Polycrystals, which induces to think that there are no important morphological differences between both samples.

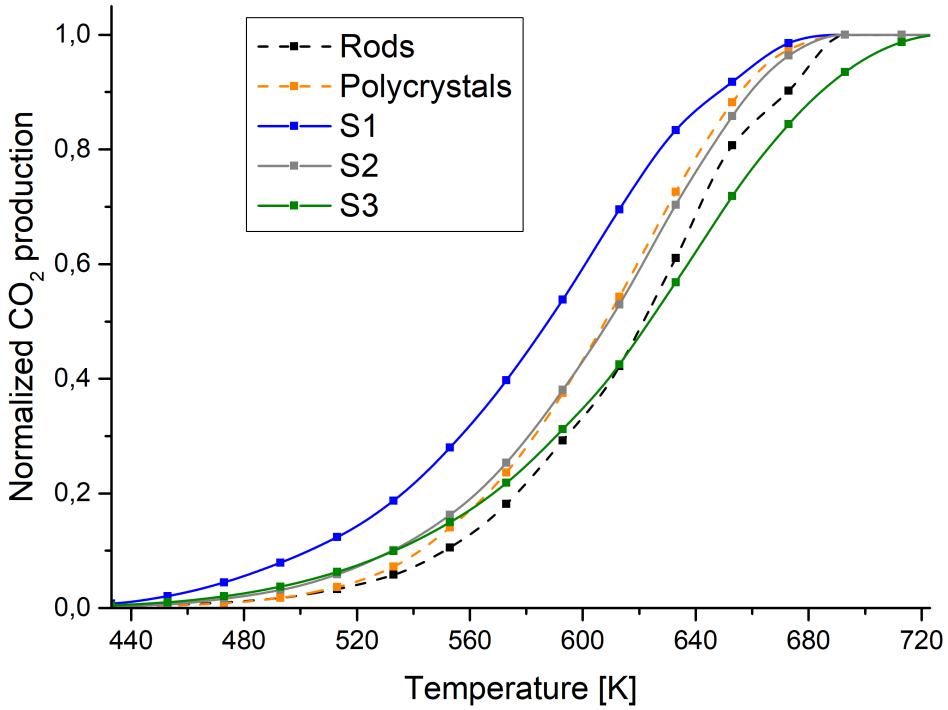

Figure 3.5: CO oxidation of bare ceria results

The differences between the morphologically similar samples S1, S2, Polycrystals and S3 can be understood taking into account that different synthesis methods most likely provide the samples with different proportions of exposed facets, low-coordinated sites at the surface (active sites) and different concentrations of vacancies at the bulk. For instance, considering the relation between oxygen vacancy concentration and lattice parameter in Table 3.1, as well as the higher catalytic activity for S1 we could make an educated guess and propose that the increased concentration of vacancies gives this sample a higher oxygen mobility.[10] Which could be expected as oxygen diffusion coefficient on ceria depends greatly on stoichiometry.[60] Given that the lower oxygen vacancy formation energy was linked with the predominant planes in the Rods sample but shows one of the lowest activities, we can discard it as a key step in the reaction for this conditions. And suggest that the limiting factor for CO oxidation in bare ceria will be oxygen diffusion. For higher conversions the availability of active sites gains importance and the results show that S3 has less active sites than the other two synthesized samples.

Finally, it can also be considered the exposed surface by the catalyst. As 100 mg where used for each sample, and rods have larger dimensions at the nanometer scale they will expose less surface than the rest of the samples. For a given concentration of active sites more surface exposure should yield a higher catalytic activity.

3.2.1 Activation energy

From a macroscopic point of view without taking into account the steps of the reaction mechanism we can consider the following reaction:

$$\mathrm{CO} + \frac{1}{2}\,\mathrm{O_2} \longrightarrow \mathrm{CO_2} \tag{3.8}$$

The rate of the reaction is defined as moles of product formed per second and taking into account the stoichiometry of the reaction we can write:

$$r = \frac{d[CO_2]}{dt} = -\frac{d[CO]}{dt} = -2\frac{d[O_2]}{dt} \tag{3.9}$$

The rate of a reaction is dependent on multiple factors. Assuming different factors such as temperature or concentrations are independent from each other we can take them into account separately. For the effects of concentration on r we introduce the concept "order of the reaction". The origin of this term comes from investigations in which it was recognized that, in many cases, the rate at a given temperature is proportional to the concentration of a reactant raised to a simple power. The sum of all the powers will be the order of the reaction.

$$r = k(T)[CO]^{\alpha}[O_2]^{\beta} \tag{3.10}$$

Where $k(T)$ is the rate constant depending on temperature, and α and β are the partial orders of the reaction. For our case of study the concentrations of reactant will be held constant at the reactor and thus the order of the reaction will not be relevant (n = $\alpha + \beta$). The Arrhenius equation is an empirical relation that gives the dependence on temperature of the rate constant. Introduced by Arrhenius in 1889 influenced by the form of the Van't Hoff equation.

$$k(T) = Ae^{\frac{-E_a}{RT}} \tag{3.11}$$

Where A is a pre-exponential factor, R the gas constant in $JK^{-1}mol^{-1}$ and E_a the activation energy of the reaction in $Jmol^{-1}$, which is considered here independent of the temperature. The activation energy would depend solely on the mechanisms of the reaction. Taking then equation 3.10 and 3.11 we can write:

$$r = A[CO]^{\alpha}[O_2]^{\beta}e^{\frac{-E_a}{RT}} \tag{3.12}$$

Redefining the pre-exponential factor taking into account the concentrations of the reactants are held constant.

$$r = Be^{\frac{-E_a}{RT}} \tag{3.13}$$

Taking the natural logarithm at both sides:

$$\ln r = lnB - \frac{E_a}{RT} \tag{3.14}$$

Considering this last equation we can extract the activation energy with a linear fitting to the experimental data relating the logarithm of the rate of the reaction and the inverse of the corresponding temperature. We present in Figure 3.6 $1000/T$ instead of $1/T$ as independent variable in order to find directly the activation energy in kJ/mol. The results of the linear regressions are depicted in Table 3.2.

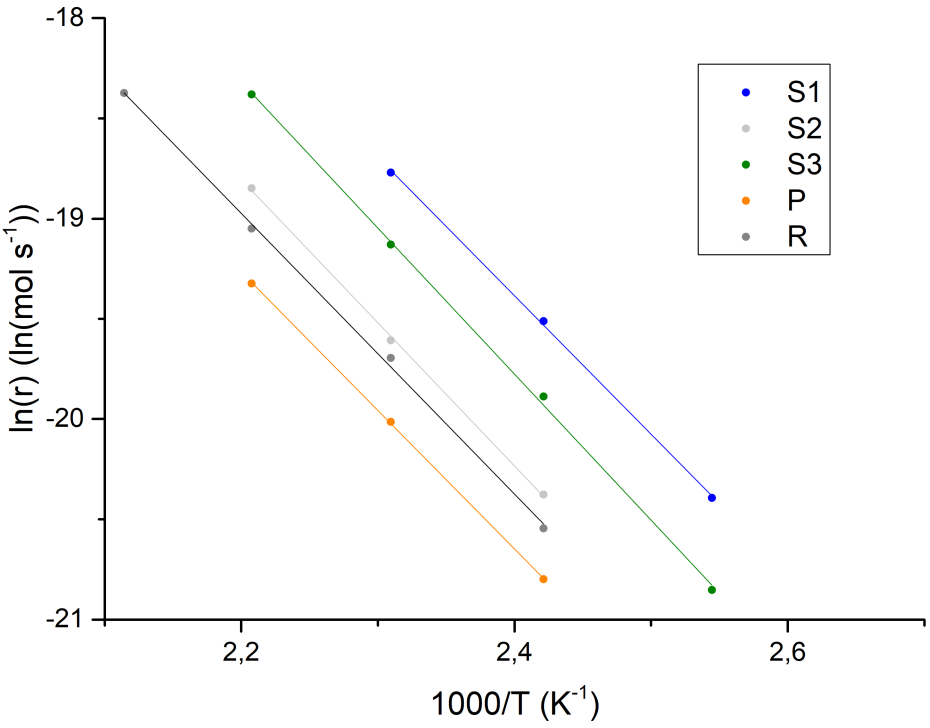

Figure 3.6: Linear fitting to experimental data of the Arrhenius equation

Table 3.2: Results of the linear regression and calculation of E_a

	Slope ($\frac{-E_a}{1000R}$)	R^2	E_a ($kJmol^{-1}$)
S1	-6.9	0.999	57.4
S2	-7.14	0.999	59.4
S3	-6.94	0.998	57.7
Rods	-7	0.998	58.2
Polycrystals	-6.91	0.999	57.4

Predictably, the activation energies for all the samples are nearly identical. As the reaction mechanism was the same and the differences between them didn't play a determinant role in this conditions.

In general, regardless of the morphology or the structure, the redox reactions with ceria can be roughly divided in two essential steps. The first one being the transport of oxygen in the bulk and the second one the surface exchange (the adsorption and desorption of species). At low CO conversions the active sites are mostly available and the limiting step is the diffusion through the bulk, diffusion through the surface or the rate of vacancy creation (sometimes called the kinetic-regime of the reaction). For higher rates of the reaction, the limiting step will be the availability of active sites and thus surface exchange will be the limiting step (which we will refer to as saturation-regime).[61] The Arrhenius equation is adjusted for each case in the kinetic-regime, for CO conversions below 15 %.

Chapter 4

AuCu/ceria catalyst

4.1 Experimental: Synthesis and catalytic test

The $Au_{50}Cu_{50}$ bimetallic NPs were prepared as described elsewhere in.[62] With face centered cubic structure, an average diameter of 2.3 nm and a narrow distribution (95 % of NP are between 2.1 and 2.6 nm). Llorca et al. measured the lattice parameter with HRTEM (High-resolution transmission electron microscopy), finding a value between that of pure gold (a_{Au}=0.4079 nm) and that of copper (a_{Cu}=0.3615 nm).[62] The AuCu/CeO_2 catalyst were prepared by incipient wetness impregnation from a toluene solution. Which contained the AuCu NPs in a 40 mM concentration. Taking the molar mass of Au as 196.9665 g/mol and the molar mass of Cu as 63.546 g/mol the alloy with a molar ratio of 1:1 should have a molar mass of:

$$\frac{\frac{196.9665}{2} + \frac{63.546}{2}\ g\ AuCu}{1\ mol\ AuCu} = 130.26\ g/mol$$

S1, S3, nanorods, and nanopolycrystals were decorated with NPs following the same method. To obtain a concentration of 1 % in weight we impregnated 150 mg of each sample with 1.5 mg of NPs which implied the use of 288 µl for each one as shown in equation 4.1. S2 sample was not used as a similar behaviour than Polycrystals was expected due to the same morphology, similar size and nearly identical catalytic activity for the test without bimetallic NP.

$$1.5\ mg\ AuCu\ \frac{1\ g}{1000\ mg}\ \frac{1\ mol}{130.26\ g}\ \frac{1000\ ml}{0.04\ mol} = 0.288\ ml \tag{4.1}$$

The 288 µl of suspension were added using an air displacement pipette to achieve a uniform impregnation for each sample. Afterwards they were placed into an oven at 673 k for 4h and then pulverized with a mortar and a pestle to achieve a good homogeneity. The four samples were tested with CO oxidation as explained section 3.1.

To have a better understanding of the transformations that take place in our catalyst one more sample was prepared. 300 mg of ceria rods were decorated with bimetallic NPs, this time instead of 1 % in weight we aimed for 3 % in order to be able to see more clearly the bimetallic NP in the XRD pattern and XPS spectrum. For the bimetallic NPs we expect to find the highest peak ascribed to its fcc crystal structure corresponding to 111 planes between that of pure gold and that of copper. Considering their lattice parameters the position of their respective 111 peaks can be calculated (The angle at which the 111 planes will produce constructive interference). From equation 3.4 we can write:

$$\theta = \arcsin\left(\frac{\lambda}{2a}\sqrt{h^2+k^2+l^2}\right) \tag{4.2}$$

In addition to the x-ray powder diffraction test an XPS study was carried out using Kα x-rays at 1486.6 eV. The photons are able to penetrate in the sample up to some micrometers, with the exact number depending on the energy of the electrons and the elements in the solid. Interacting in this way with the different atoms of the sample through the photoelectric effect. The photoelectrons produced in the process may escape the solid with a certain kinetic energy E_k and reach the detector.

$$E_k = h\nu - E_b - \phi \tag{4.3}$$

Where $h\nu$ would be the initial energy of the photons (1486.6 eV), E_b the binding energy to the nuclei and ϕ the work function of the spectrometer (the difference between the Fermi energy and the vacuum energy). As the electrons will lose energy rapidly the mean escape depth will be small, of the order of tens of Angstroms (much smaller than the penetration depth). More precisely, the signal that is received from the detector can be considered to come from a depth smaller than three times the IMFP, which is the inelastic mean free path or the average distance that electrons travel without having an inelastic collision and losing energy.[63,64] This can be understood taking into account that the contribution to the intensity of photoelectrons coming from a depth r (measured perpendicular to the surface) is given by Beer-Lambert law (equation 4.4).

$$I = I_0 e^{-r/\lambda} \tag{4.4}$$

We can calculate the total intensity integrating for all depths and compare that value with the integration up to a depth 3λ (I_s):

$$I_T = \int_0^\infty I_0 e^{-r/\lambda} dr = I_0\lambda \qquad I_s = \int_0^{3\lambda} I_0 e^{-r/\lambda} dr = 0.95 I_0\lambda \tag{4.5}$$

Therefore it is clear that 95 % of the signal arriving at the spectrometer comes from the first 3λ nm of the sample, being the contributions more important as we approach the surface. Tanuma et al. calculated the IMFP for different elements and

x-ray energies.[65] Obtaining for 1500 eV x-rays $IMFP_{Au} \sim 1.7$ nm and $IMFP_{Cu} \sim 2.2$ nm. Although some authors have reported that the maximum escape depth for that x-ray energy in bimetallic nanoparticles is ~ 2.5 nm.[66]

Moreover, during the analysis, some samples tend to accumulate a stationary charge. This charge modifies the position of the peaks and has to be corrected using some well-known peaks, typically C 1s. Also, it has to be taken into account that in heterogeneous samples, different materials may acquire different charges and thus must be compensated differently. Deconvolution and processing of the peaks was carried out using the CasaXPS software. The compensation for the static charge was made using the $3d_{5/2}$ and $3d_{3/2}$ cerium lines for all the spectrum and an additional calibration with $1s$ carbon line for gold and Ce 4s for oxygen.

4.2 Results

The same experiment carried out for the samples without metallic nanoparticles was conducted for the decorated ones, using the same set up as described earlier. The results of which are shown in Figure 4.1. One of the more noticeable differences was the much higher activity at low temperatures with respect to bare ceria. The best results were obtained for AuCu/Rods with 92 % of CO conversion at 373 K (100°C). Followed by S1, Polycrystals and S3. The point in which the production of CO_2 as a function of temperature is non-differentiable can be understood as a change in the catalyst structure ("activation") which will be explored more deeply afterwards. The values of the temperature for 50% and 100% of CO conversion (T_{50} and T_{100}) are shown in Figure 4.2. Where the remarkable enhancement of ceria as catalyst can be clearly seen.

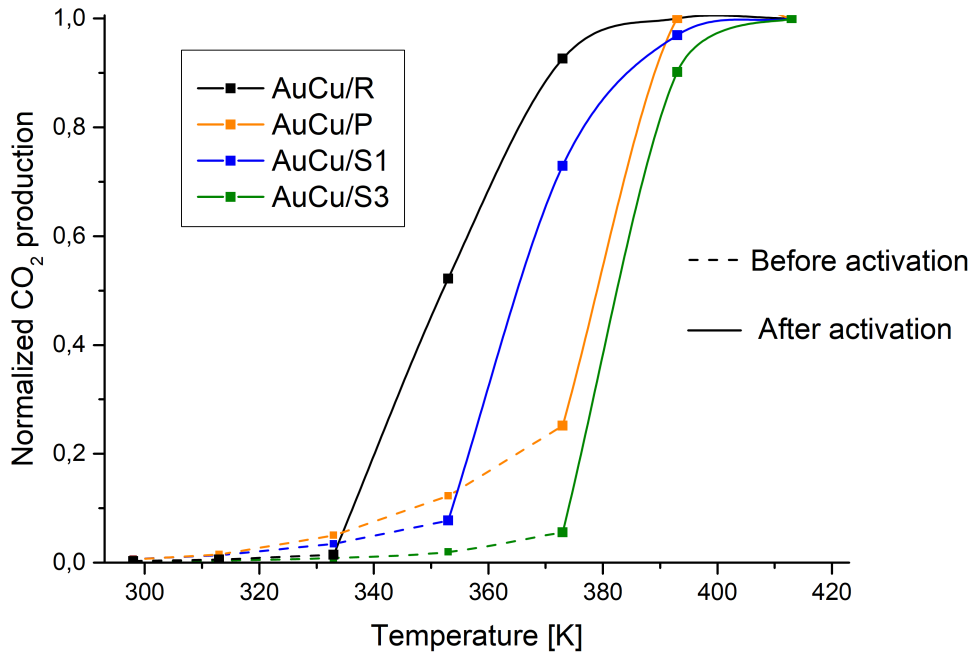

Figure 4.1: Results for CO oxidation of the bimetallic catalysts over different ceria samples

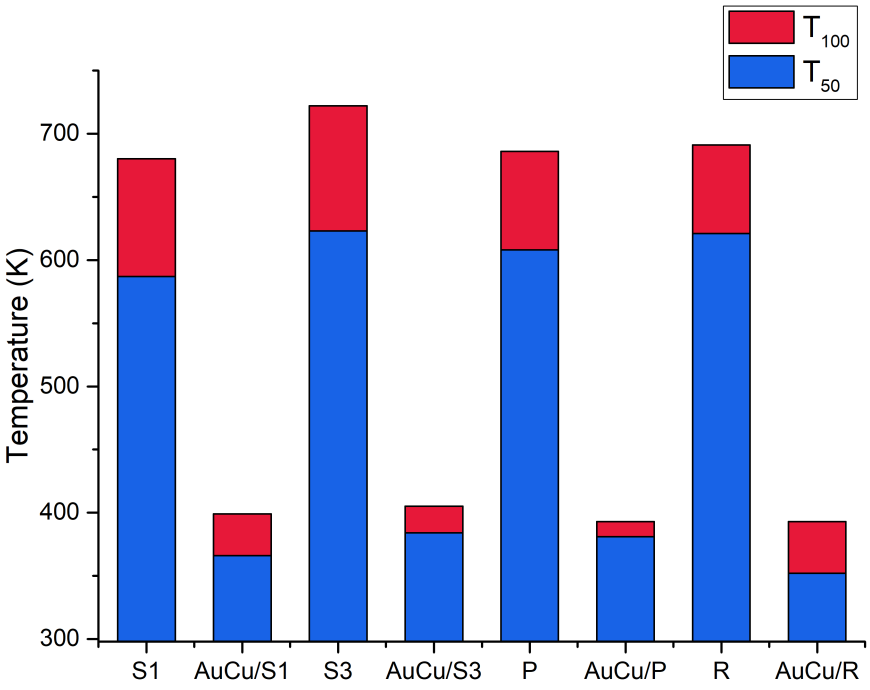

Figure 4.2: Comparison of catalytic activity between bare ceria and ceria with metallic nanoparticles

The results present differences in $\mathbf{T_{100}}$ between the decorated and the pure ceria samples of 300 K in average. With the highest difference observed for S3 and the lowest for S1. With the former presenting a reduction in the activation energy of 63 %. As it is shown in Figure 4.3. In addition, with a closer look at the results it can be noted that the differences in T_{100} between the AuCu/x samples are smaller than the variations in T_{50}. Which can be understood taking into account that the activation temperature (and thus the reach of higher conversions) was morphology-dependent as will be explained and took place in the kinetic-regime, while the complete conversion of CO occurred in the saturated-regime (which was alike for all the samples due to the similar structure).

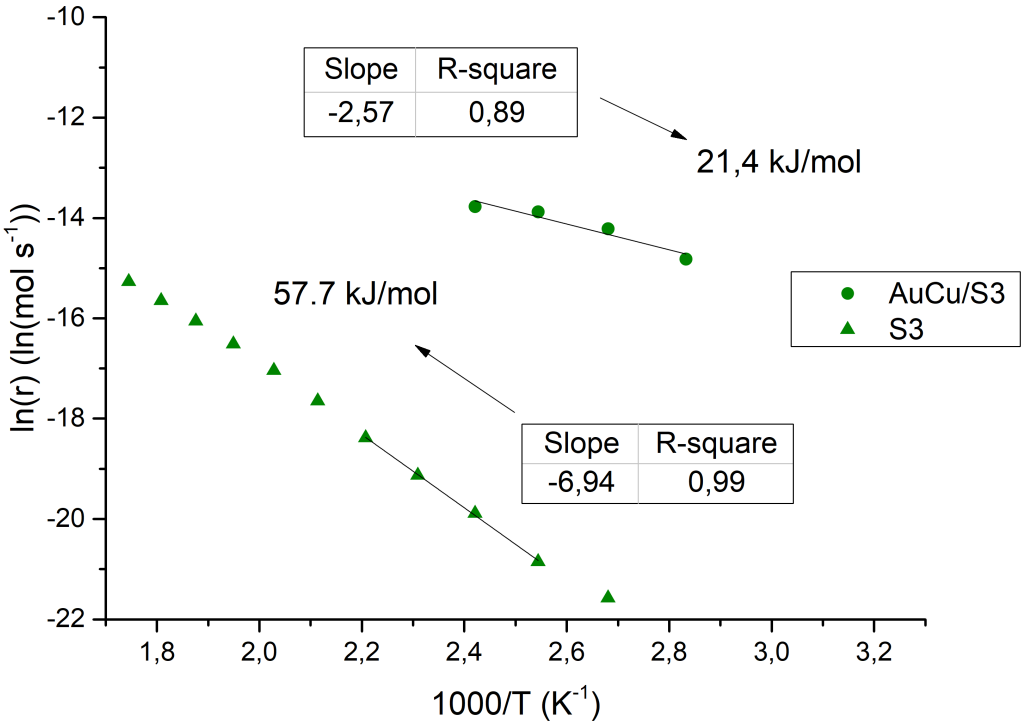

Figure 4.3: Activation energy from the fitting of experimental data to the Arrhenius equation.

As the bimetallic NP were the same for all the samples, the overall improvement in catalytic activity at low temperatures should be ascribed to the synergistic effect between ceria and the bimetallic AuCu nanoparticles while the differences between them should be related to the distinct synthesis methods for the ceria support. Which now, in the presence of AuCu NP will not have the same effect as with bare ceria at higher temperatures. Given that the limiting factors of the reaction change with the variations in the catalytic system and conditions, is comprenhensible that the order in catalytic activity is not mantained with respect to the previous experiment. Being now AuCu/R the most active one followed by AuCu/S1, AuCu/P and AuCu/S3.

In a previous study Au/CeO_2 catalyst where synthesized and used in CO oxidation.[42] Among the different samples used as support the rods and polycrystals used in this previous experiments were tested. Yielding the following results for CO oxidation:

Table 4.1: Catallytic activity of Au/Rods and Au/Polycrystals extracted from[42]

	Au/R	**Au/P**
$\mathbf{T_{50}(K)}$	361	405
$\mathbf{T_{100}(K)}$	433	>453

Which seem to present a slightly lower activity than the rods and polycrystals decorated with AuCu in this work. However, a direct comparison should not be made due to the fact that the loading and size of metallic nanoparticles was different. The Au NP of Table 3.2 had a diameter between 4.5-5.5 and were loaded in a 0.25 % wt.[42] While the bimetallic NP of this study were loaded in a 1 % wt. and had an average diameter of 2.3 nm with a narrow distribution before calcination, as mentioned before.

4.2.1 Activation of the catalyst

Another remarkable difference with respect to the bare ceria experiments was the time used by the system to reach steady state for a given temperature. For example, if we compare the sample S1 in CO oxidation before and after decoration with bimetallic NPs, there is a clear difference in the amount of time consumed to reach equilibrium. In Figure 4.4 we observe that for each change in temperature the system took an hour to reach a constant value of CO_2 at the entrance of the GC. While in Figure 4.5 it can be shown that at a certain temperature the system took more than a day to reach equilibrium. The exact temperature at which activation took place varied between the different supports and are presented in Table 4.2. This delay in the dynamics of the reaction was ascribed to a structural change in the catalyst involving the bimetallic NPs. Another hint which supported this hypothesis was the difference in performance once activated. Observed in Figure 4.5 and even more clearly in Figure 4.6. As the experiments were too long to be carried out in a single day, in some cases the oven was cooled during the night and started again on the next morning. And for the sample AuCu/S1 it can be clearly seen how at the next day the system reached in half an hour for 373 K a level of activity that took the previous day more than 3 hours (Figure 4.4).

Table 4.2: Comparison of the approximated activation temperatures between samples

	AuCu/S1	**AuCu/S3**	**AuCu/P**	**AuCu/R**
$\mathbf{T_{act}(K)}$	373	393	< 393	353

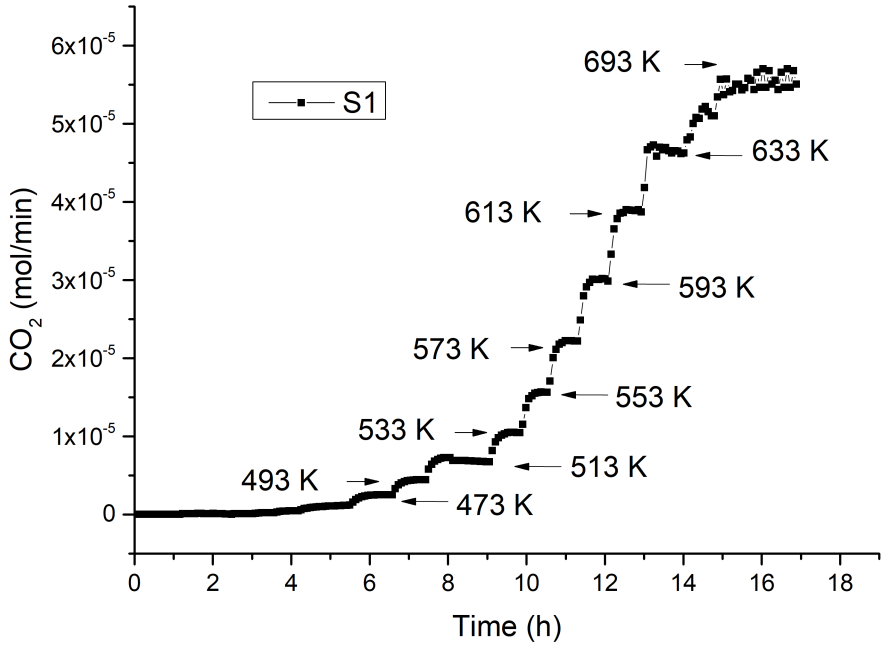

Figure 4.4: CO oxidation experiment for S1 (bare ceria)

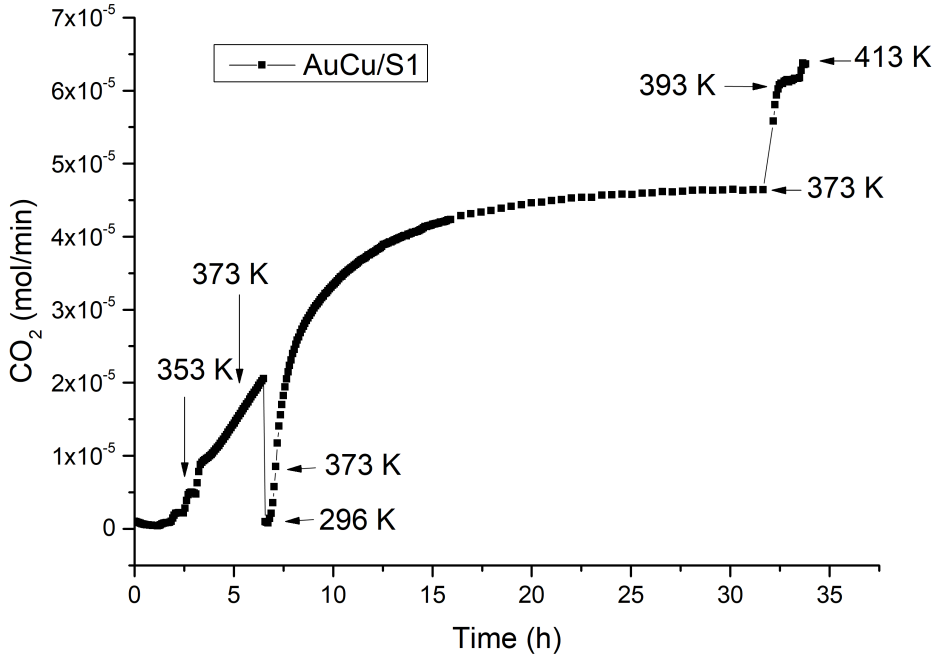

Figure 4.5: CO oxidation experiment for AuCu/S1

Figure 4.6 gives further support to our previous hypothesis with a clear hysteresis between the heating and cooling ramps in the experiment for AuCu/S3 (which could

have been observed probably in the rest of samples). A much higher activity is shown by the catalyst for each temperature once it has been activated, this time at 393 K. Other studies have also reported this kind of hysteresis between the heating and the cooling ramps attributing it to a change in the catalyst structure.[67]

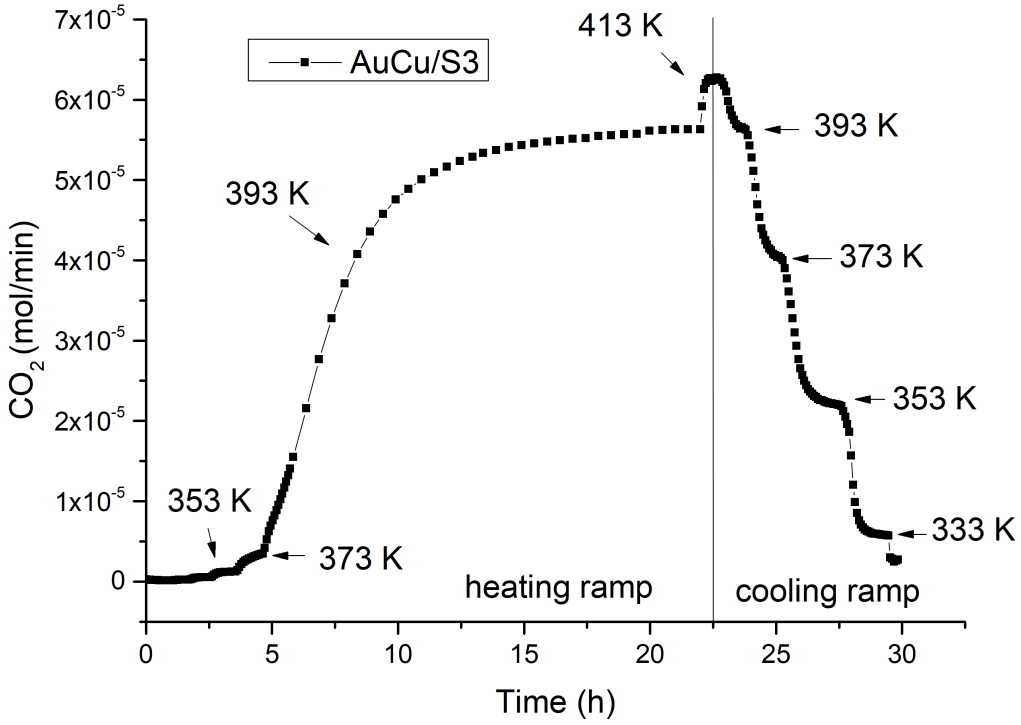

Figure 4.6: CO oxidation experiment for AuCu/S1

4.2.2 Structural changes

Equation 4.2 give us the value of θ in radians, converting to degrees and multiplying by a factor of 2 we obtain the interval in which we should find the peak corresponding to an alloy of the two metals. Yielding 38.17° for Au and 43.29° for Cu. Where we are carrying the error made in the calculation of the lattice parameter. A change in 0.002 Å in the later will cause a change of 0.05 °. So the second decimal should probably not be taken into account.

As the original signals were very noisy a convolution was carried out using 150 points of a fifth degree polynomial (Savitzky-Golay method) with the Analysis tool Origin. Subsequently the peak was identified and as we can see in Figure 4.7 is nearly non-existent. This might be for two non-excluding reasons. The first one is that a 3% in weight with so small NP might not be enough to yield an intensity higher than the noise of the instrument, and thus the peak is nearly overlooked. The second has to do with the fact that during calcination, part of the metallic Au and Cu atoms may have entered the ceria lattice and thus doped the catalyst. In this

case, they will diffract just as the fluorite structure and won't yield any intensity in the mentioned interval whatsoever. This second hypothesis would be supported if a change in the lattice parameter was observed with respect to bare ceria rods, given that Cu atoms have a much smaller radius than Ce and Au atoms have a slightly smaller radius too. Using once more equation 3.4 we can extract the lattice parameter from the XRD pattern and compare it with the one we had for Rods.

Which yielded in this case a value of 5.4175 Å, which is slightly smaller than the one found for bare ceria 5.4188 Å. Although the reduction in the lattice parameter points out to the doping of ceria, the change in the lattice parameter is so small we have to consider if it is relevant at all. For instance, the propagation of uncertainty has to be taken into account to see if the observed variation is greater than the expected uncertainty for the lattice parameter. Considering the following function:

$$a = \frac{\lambda}{2sin\theta}\sqrt{h^2 + k^2 + l^2} = a(\lambda, \theta) \tag{4.6}$$

$$da = \left|\frac{\partial a}{\partial \lambda}d\lambda\right| + \left|\frac{\partial a}{\partial \theta}d\theta\right| \tag{4.7}$$

Where the partial derivatives are evaluated at the values measured.

$$da = \left|\frac{\sqrt{3}}{2sin(\theta)}d\lambda\right| + \left|\frac{\sqrt{3}\lambda cos(\theta)}{2sin^2(\theta)}d\theta\right| \tag{4.8}$$

Taking as $\lambda = 1.54$ Å, $\theta = 0.333265$ rad (which is half of the measured 38.1894° in radians), $d\lambda = 0.001$Å and $d\theta = 8 \times 10^{-5}$ rad (which is half of the 0.01°angle step in radians). We obtain an uncertainty for the value of the lattice parameter calculated with equation 3.4 of ~ 0.004. Given that the uncertainty of our measure is greater than the difference between the lattice parameter of rods and the one of bimetallic NP on rods we can't extract any reliable conclusions from this change in a.

Moreover, we can make a rough estimation on what would be the expected change in the lattice parameter if the Cu species of the NP had doped the ceria support completely. Considering the geometry of the fcc lattice of ceria:

$$4r_{Ce} = \sqrt{2}a \qquad r_{Ce} = \frac{\sqrt{2}a}{4} \tag{4.9}$$

Taking the lattice parameter of rods we obtain a cerium radii (r_{Ce}) of 1.916 Å, which is between the ionic (1.11 Å for Ce (IV)) and covalent radii (2.04 Å) for cerium, taken from WebElements. Supposing the ceria has been doped uniformly, the 3% in weight of AuCu NP would correspond to a certain number of Cu moles that would yield a certain proportion of substituted Ce cations. The molar fraction x of Cu/(Ce + Cu) is ~ 0.0194. And considering again the relation for the fcc lattice we would expect the new lattice parameter to be similar to:

$$a = \frac{4}{\sqrt{2}}((1-x)r_{Ce} + xr_{Cu}) = 5.386 \text{ Å} \tag{4.10}$$

Where the covalent radii of Cu (1.32 Å) has been used instead of the ionic (0.68 Å) to over-estimate the lattice parameter value, again from WebElements. This estimation agrees well with the lattice parameter of $Ce_{0.975}Cu_{0.025}O_2$ found by Aranda et al. (5.397 Å). For which they observed a change in the lattice parameter of 0.018 Å with respect to stoichiometric CeO_2.[68] Although another study done by Kim et al. reported a change of 0.008 Å between CeO_2 and $Ce_{0.95}Cu_{0.05}O_{2-\delta}$,[69] is still way smaller than the difference found in our samples (0.0013 Å). Thus concluding that the difference observed in lattice parameter does not constitute reliable proof of the Cu atoms entering the ceria lattice. An educated guess can be made, claiming that at most, a small fraction of the total Cu loading may have entered the lattice. But the majority of the copper loading stayed on the surface after calcination.

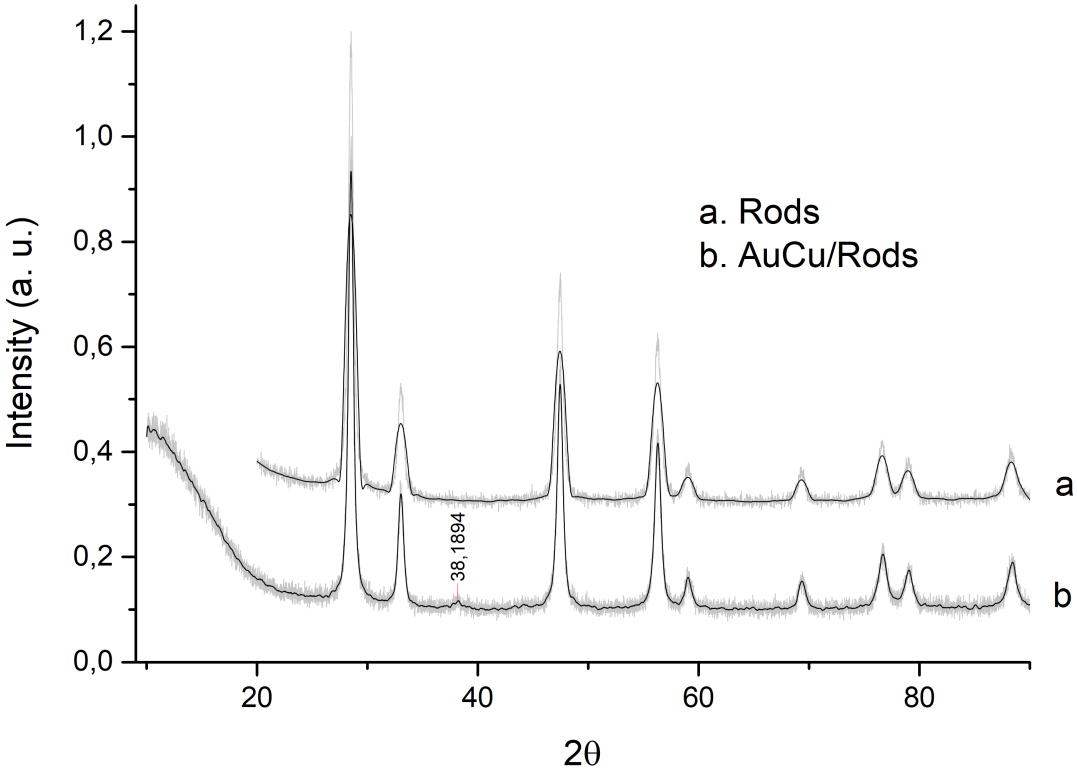

Figure 4.7: XRD pattern of the 3% AuCu decorated Rods before reaction.

Nevertheless the diffraction peak corresponding to the allegedly bimetallic NP is far more close to the peak corresponding to Au 111 than to the Cu 111 peak. Which induces to think that the copper species are not located in the NP as part of the alloy, but segregated to the interface with the support, the core of the NP or elsewhere. This results are in agreement with some studies which, after calcination,

found that the Cu species had migrated from the metallic NP and were present as CuO clusters, either amorphous or too small to be observed by XRD.[56,58] Also with some studies that reported to observe only the shell element in XRD patterns with core-shell bimetallic structures.[70] The hypothesis made here may be later confirmed with the XPS results. Either the doping of the lattice or the migration of Cu species to the surface support coincides with previous results on AuCu NP. As some of them have doped ceria with Cu[69,71] and the ones that used AuCu bimetallic NP did not use ceria as support and found CuO species migrated from the Au NP.[58,67,72]

At this point two structures can be discarded after calcination. AuCu alloy NP supported over ceria (as it will yield a diffraction peak closer to the one corresponding to Cu 111). And Au NP with CuO patches, as this structure would be active for low temperature CO oxidation from the start. What is clear is that our AuCu bimetallic NP have suffered some phase segregation during calcination and that Cu species are either amorphous or too small to produce a diffraction peak such as the one produced by Au clusters left behind.

The XPS spectrum shows lines corresponding to cerium, oxygen, gold, carbon, which is always present due to hydrocarbons introduced from the laboratory environment and no other major contaminants whatsoever. Unfortunately, the lines corresponding to Cu are overlapped with a shake-up from cerium, thus making difficult the extraction of quantitative results. In some cases, there is a certain probability that after ionizing the atom, the ion ends up in an excited state, and thus the photoelectron reaches the detector with less energy (kinetic energy of the electrons) than they normally would for that element. Whenever this probability is high enough we obtain the apparition of lines at a higher energy (binding energy of the electrons to the nuclei) than the corresponding binding energy to that element. Called shake-up lines and found for Cerium and also for copper as we will see.

The spectrum reveals Au lines at 88.1 eV and 84.6 eV for $4f_{5/2}$ and $4f_{7/2}$ respectively. With a difference in energy between them of 3.58 eV, which is similar to the theoretical value $\Delta E = 3.67$ eV.[73] As it is shown in Figure 16. In general, the binding energies of NP exhibit a shift with respect to bulk samples, even more so when forming alloys.[74] As an example, Kim et al. reported that pure metallic Au NP without support exhibit the $4f_{7/2}$ line at 84 eV[75] while $AuCu_3$ showed the same line at 85 eV. Moreover, it has to be taken into account the support dependence. While for pure metallic Au NP without support exhibit the $4f_{7/2}$ line at ∼84 eV,[75,76] supported on CeO_2 show it at 84.5 eV[77] and supported on TiSi (Titania-Silica) at 83.1 eV.[78] Taking this into account is reasonable to assume that we have Au in its metallic state, with the shift to higher binding energies ascribed to the effect of having NP and maybe Cu species remaining in the NP.

Ce 3d is fitted correctly taking into account the presence of the two lines $3d_{5/2}$ and $3d_{7/2}$ for both Ce(III) and Ce(IV) species. In the case of Ce(IV) this is complicated by the fact that there are three possible final states for the ionized Cerium and thus the two lines corresponding to the spin-orbital doublet become 6. While for Ce(III) there are only two possible final states, therefore 4 lines.[79] As it can be seen from Figure 4.8 Taking into account the relative areas of each line and summing all the contributions for each cerium oxidation state we obtain 17.4 % of Ce(III) and 82.6

% of Ce(IV).

O 1s is deconvoluted into two different peaks in Figure 15. The first one at 528.73 eV is normally ascribed to CeO_2 lattice oxygen as reported by Mullins et al.[79] The second one at 530.93 eV is assigned to ($-$OH) groups at the surface by some studies of XPS analysis of ceria, which may come from background H_2O.[80,81]

This results give us information about the first nanometers of our sample. Specifically, for the Au NP the mean escape depth of the electrons is expected to be $\sim$ 2.5 - 5 nm as explained before in section 4.1 (where 5 nm come from 3 times 1.7 nm which is the IMFP for photoelectrons from 1500 eV x-ray in Au). And thus, in the case of NPs smaller than $\sim$ 5 nm we would expect that the XPS technique would clear the entire composition. However, as reported by Llorca et al., the bimetallic NP experience some growth during calcination. Which is proportional to the calcination temperature and the NP loading on the support. For our case, the NP are expected to have a mean diameter of $\sim$ 6 nm if we don't take into account the different supports used in this work and in the reference article (CeO_2 and TiO_2).[62]

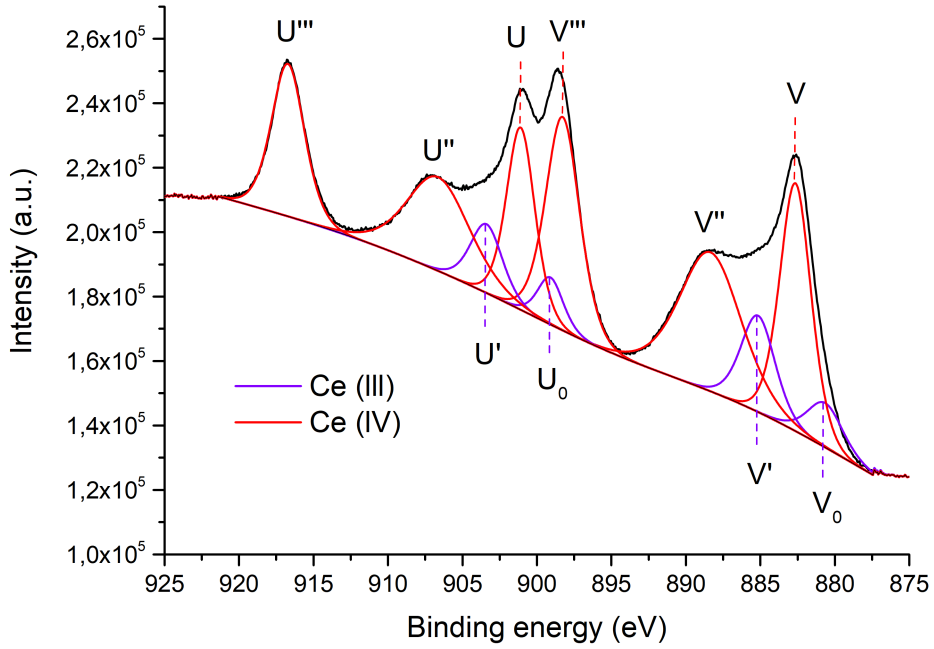

Figure 4.8: XPS spectrum showing Ce $3d_{5/2}$ and Ce $3d_{3/2}$ of the two possible oxidation states of Ce in cerium oxide.

The lines corresponding to Cu species were too weak to extract any reliable data taking into account that the low level of the signal could be due to the low metal loading of the sample. Even though the same atomic loading was carried out for both metals, the cross-section for both elements at the used x-ray energy is different. This cross-section for emission is the probability of extracting an electron due to the incoming radiation, which is dependent on the element, the orbital and the energy of x-rays.[63] In addition, the lines corresponding to the $2p_{3/2}$ lines of different copper oxidation states are very close together between 934 eV and 932 eV, followed by shake-up lines of the Cu (II) oxide and the $2p_{1/2}$ lines.[82] What is clear from Figure 4.9 is that the difference between them is minimal, and thus should be able to discard any major changes in the Cu species in the first nm of our sample.

In order to properly understand the difficulty in obtaining quantitative results as well as confirming the presence (although minimal) of a line corresponding to Cu species, two XPS spectrum of bare ceria are compared to the post-reaction sample in Figure 4.10. The difference between them can be clearly seen as the binding energy corresponding to Cu species is slightly higher than the shake-up coming from cerium.

The calibration for the post-reaction XPS spectrum was carried out using the same elements as in the pre-reaction spectrum for each line. Au lines after reaction shifted to 84 and 87.6 eV for $4f_{7/2}$ and $4f_{5/2}$ respectively. A variation in the binding energy is usually ascribed to the the removal or adding of electronic charge due to a change in bonding. And thus a decrease in the binding energy represents a transfer of electronic charge to the Au atoms (possibly due to a change in their chemical environment as will be later discussed). Still we can consider we have metallic Au although with a different environment as mentioned.

Ce lines were fitted as explained for the pre-reaction spectrum. Finding this time a proportion for each Ce oxidation state of 13.3 % and 86.7 % for Ce (III) and Ce (IV) respectively. Which is very similar to the one found for pre-reaction conditions taking into account the difficulty of adjusting perfectly the 10 merged peaks of Ce $3d_{5/2}$ and Ce $3d_{3/2}$.

O 1s is deconvoluted in the same way yielding the main line at 529 eV (which is in the range of energies for metal oxide as before) and the one corresponding to (-OH) groups at 531.13 eV. So no important changes are observed in oxygen species.

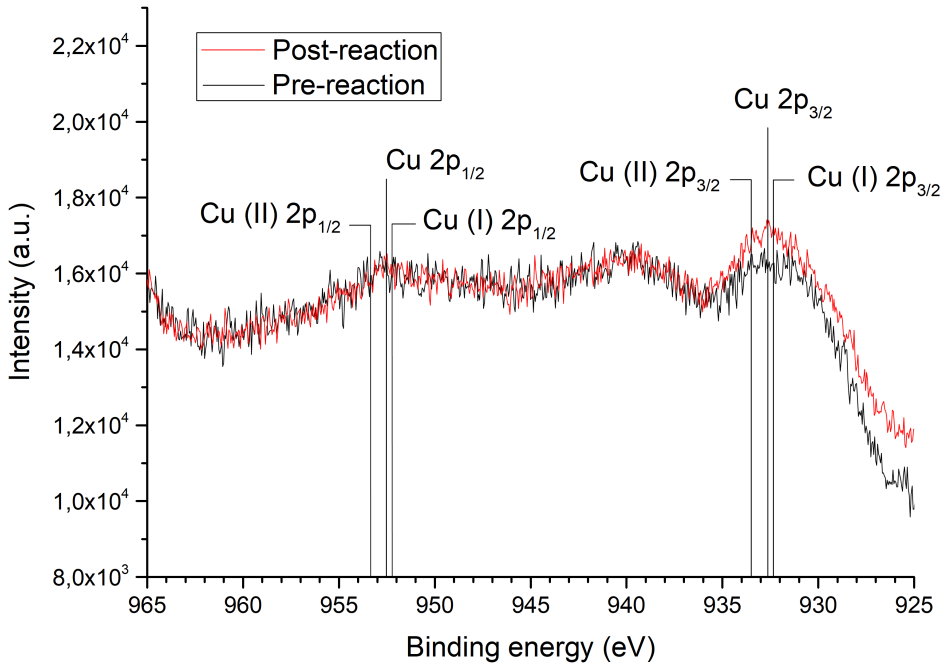

Figure 4.9: Pre-reaction and post-reaction lines of Cu.

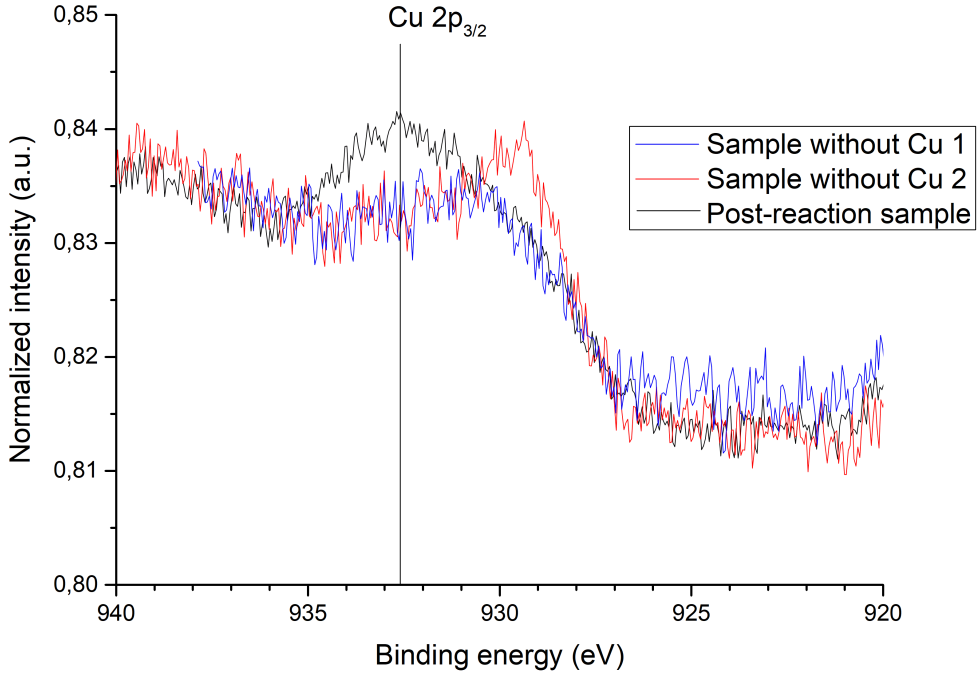

Figure 4.10: Comparison between bare ceria samples and samples with ceria and Cu

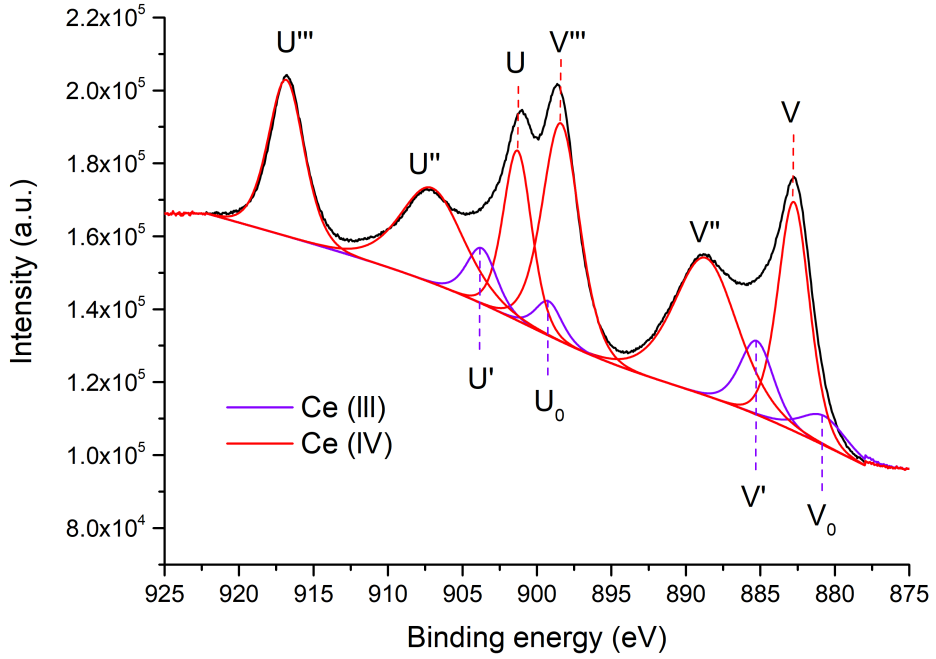

Figure 4.11: Post-reaction XPS spectrum showing Ce $3d_{5/2}$ and Ce $3d_{3/2}$ of the two possible oxidation states of Ce in cerium oxide.

With this information into account we can devise a pre-reaction scenario in Figure 4.12. Discarding those structures we know that are not compatible with either the results, the XRD pattern or the XPS spectrum. As explained before the initial average diameter of the NP **a** was $\sim$ 2.3 nm. After calcination, the expected size of the NP is **c** $\sim$ 6 nm and the XRD pattern showed Au NP.

All in all, we have discarded that a major fraction of the Cu loading has entered the lattice due to the discussion made previously with the lattice parameter. Also, we have ruled out the possibility of having the copper alloyed with gold in the NP due to the position of the NPs peak in the XRD pattern. Moreover, given that there are no important changes between the pre- and post- reaction lines of Cu we can assume that the Cu atomic fraction is similar. Assuming that the final structure after activation is the one reported in the literature and mentioned in section 1.7 (which is the one known to be active for CO oxidation), we can probably discard migration of all the copper loading upon reaction conditions from the core to the surface of the NP. If that was the case, the differences between the pre- and post- reaction spectrums for Cu would have been greater. Nevertheless, as the quantification of surface Cu cannot be conducted this is only an educated guess and the possibility of having important surface segregation upon reaction conditions should not be totally ruled out. Finally, as the results of the experiments presented in section 4.2.1 point out to a transformation of the catalyst and were not active from the start, the possibility of having CuO species in contact with the NP before the reaction is also dismissed. Leaving us with the two options depicted in Figure 4.12. Where the Cu species are probably Cu oxide formed during calcination in air. As those conditions

are more favorable to oxidation than the reaction gas mixture, considering there was a higher proportion of CO than O_2.

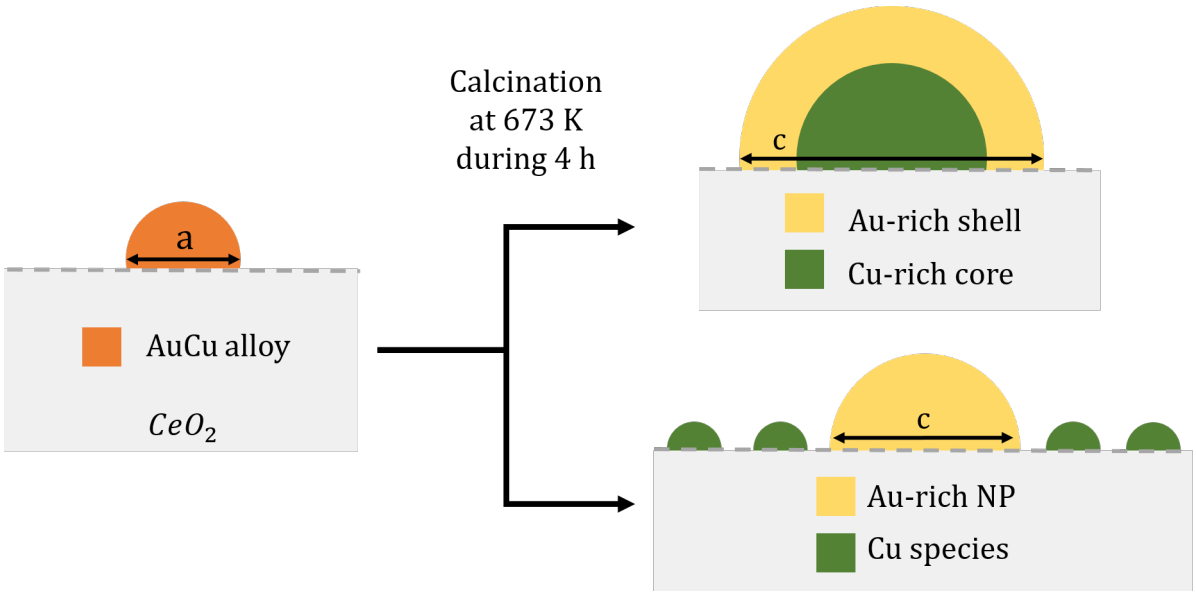

Figure 4.12: Pre-reaction depiction of the catalyst structure based on the characterization and experiments results.

As for the XRD pattern after reaction the results show a shift in the NP 111 peak as well as the ceria 111. For cerium oxide we found now the 111 peak in $2\theta = 28.4°$while for the metallic NP we found $\sim 38.1°$which is ascribed to pure Au NP. Carrying out the same procedure as done for the XRD pattern before reaction and using equation 3.4 once more we obtain a lattice parameter $a = 5.437$Å which is an important increase with respect to the lattice parameter before reaction ($a = 5.418$Å). The shift of the NP peak may be ascribed to the segregation of the remaining Cu species in the Au clusters to the surface under reaction conditions (several examples of such phase segregation are found in the literature as will be mentioned). As for the increase in the lattice parameter one possible explanation would be the depletion of oxygen in the bulk during reaction. The increase in oxygen vacancies in the bulk (while the concentration in the surface has decreased) would provoke an increase in the lattice parameter as we have already seen. Although this is only a hypothesis and none of the results support this claim in particular.

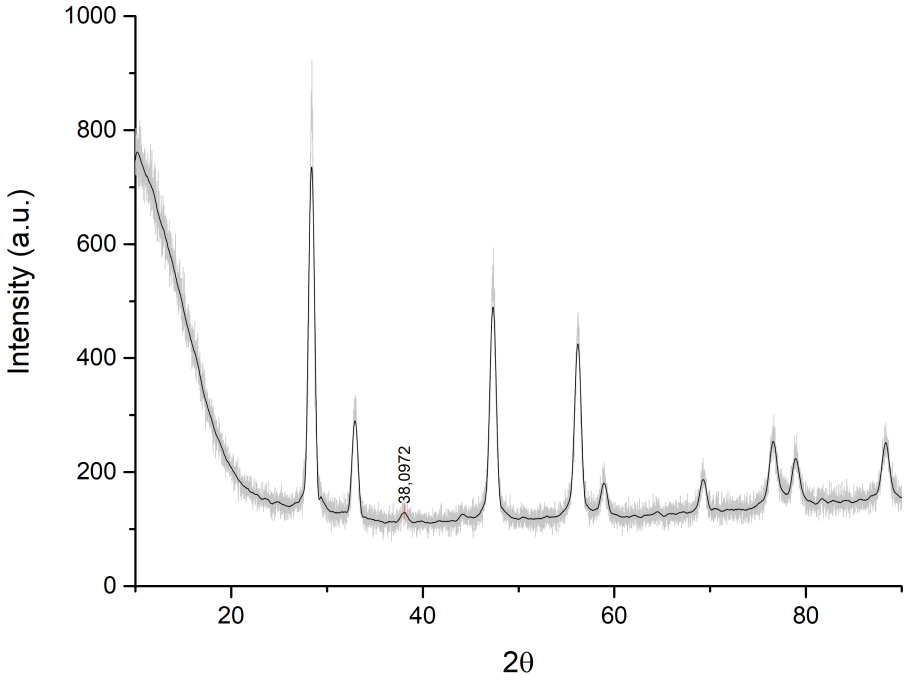

Figure 4.13: XRD pattern of the 3% AuCu decorated Rods after reaction.

4.3 Final discussion

Considering the mentioned literature and the results of this work, it is reasonable to think that upon calcination in air metallic Cu atoms were oxidized and driven to the support surface or even to the core as mentioned earlier. The exposure of the catalysts to the reaction atmosphere induced a structural change linked with the migration of CuO species from the support (or core) to the Au NP surface in strong interaction with gold.[56] Which could be attributed to the presence of CO, given that the catalysts were calcined at 673 K in air without activating. Several other examples of metallic surfaces reconstruction or CuO species migration under CO exposure and reducing atmospheres can be found in the literature.[57,67,83] This phase segregation has proven to be size and support dependent among other factors in several theoretical and experimental studies[56,67] agreeing with the results presented in this work. Exposure of bimetallic NP to reactive environments can cause surface segregation, dealloying and selective oxidation as reported by Destro et al.[67] In fact, surface segregation is a common phenomenon for bimetallic catalysts, and is influenced by the properties of the two components such as bond strengths and surface energies and also affected by external conditions such as temperature and composition of the atmospheres during the pretreatment and reaction steps.[58]

It has been shown several times that CO does not adsorb strong enough onto Au–Cu alloy nanoparticles compared to Au nanoparticles and thus without the creation of CuO we would observe less catalytic activity for AuCu/Rods than for

Au/Rods.[55,56,84] Supported by the fact that before activation, at room temperature, the observed catalytic activity is negligible. It has been reported by Bauer et al.that the activity of the bimetallic system starts to increase at the temperature at which the migration of Cu ocurred.[56,84] This CuO species would facilitate the adsorption and activation of gas oxygen and stabilize the gold nanoparticles as mentioned before.[55]

Therefore, taking all this information into account, a mechanism for CO oxidation can be proposed. Where Au or AuCu sites would be responsible for the adsorption of CO while CuO and the ceria surface would strongly bind and activate oxygen gas species. The support would also be responsible for the segregation of Cu at low temperatures in the reactive environment, as other studies which used different supports other than ceria have reported activation by the same mechanism but at much higher temperatures.[67,72] And considering the correlation established between oxygen vacancy formation energy at the surface and activation at lower or higher temperatures, we introduce here a possible explanation. The samples with the lowest vacancy formation energy are the ones that enabled the migration of Cu oxide at lower temperature, that is to say Rods. Oxygen vacancies at the surface would increase surface diffusion. Among the rest, the order of activation follows the same order of catalytic activity of bare ceria. Which depended strongly on oxygen mobility and the possible different proportions of facets exposed (directly related with the redox properties of each sample).

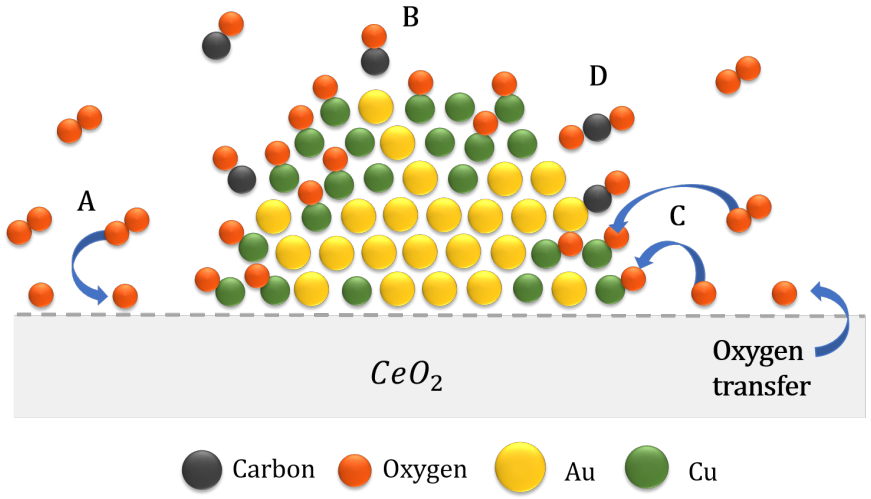

Figure 4.14: Scheme of the reaction mechanism proposed for AuCu bimetallic NP supported on ceria

In this case, the interface between Au or AuCu and CuO is considered as the active region of the catalyst. CuO_x would provide the activated oxygen species (C) while CO would preferentially adsorb onto Au atoms (B) (although in some reports CO adsorption onto Cu and O adsorption onto Au have been reported as well[71]). The adsorbed CO would react with activated oxygen on CuO_x (D). This oxygen would be regenerated by lattice oxygen and gas oxygen species.[67] The reduced competition of the reactants for the binding sites is one of the characteristics that grants this system with a good catalytic activity as predicted by DFT in some reports.[85]

The formation of CuO clusters in strong interaction with Au metallic species enhanced the catalytic activity. However, this synergistic effect is highly dependant on the CuO coverage degree of the Au-rich core. Which in turn depends, for a given support, on the Au/Cu ratio.[56,57,72] Taking into account the reaction mechanism proposed above, it is reasonable to think that the best ratios will be those which yield at the end partially covered Au-rich cores. As the catalytic activity will be inhibited for totally covered ones. Moreover, the smaller the CuO patches, the higher ratio between atoms at the interface and total metallic loading, thus boosting catalytic activity.[58]

Conclusions

The synthesis and characterization of different ceria samples was carried out. Despite the fact that in all cases the most stable thermodynamic morphology was produced, the reaction tests showed different levels of catalytic activity and oxygen mobility for each one. Which has been determined as the key factor for understanding the differences between bare ceria samples in CO oxidation. Being the most active one S1.

Preformed AuCu NP were deposited through wetness impregnation to enhance the catalysts by modifying the reaction mechanism. The catalytic performance of all the samples increased strongly. And clearly, the activation and creation of the active structure was support dependent. Also support dependent, although in a smaller extent, was the catalytic performance after activation (considering the T_{100} value as a measure of performance). The posterior characterization was conducted successfully. Which allowed the elucidation of the main structural changes that took place and the reaction mechanism behind the increase in activity with respect to bare ceria samples.

Based on this findings and on the bibliography research, it is possible to devise the future steps that should be taken in order to further improve the catalytic system

Future prospects

In regards of the main work presented here, several changes could be implemented to improve the results that support the hypothesis presented here. For instance, as we have already mentioned, during the synthesis that were carried out the most stable morphology was obtained. A more compelling outcome would have been the obtainment of different morphologies with well defined facets. In order to discern precisely the exposed crystallographic plane effect on the formation and performance of the $CuO/Au/CeO_2$ catalyst. In addition, the XPS studies were not conclusive with respect to the Cu surface concentration due to the difficulties mentioned. Several ways of avoiding those difficulties would be to increase the metallic NP loading even more (supposing the same transformation took place), using different x-ray energies the signal from Cu species cold be emphasized (as the cross-section was dependent on the energy of the incoming radiation).

As far as the activity of this bimetallic catalyst is concerned, it could be im-

proved in several ways. For instance, a study by Wangcheng Zhan et al. stated that the crystal structure of the AuCu nanoparticles played an important role too. And demonstrated that face centered cubic (fcc) and face centered tetragonal (fct) structures showed remarkable differences in phase segregation and catalytic performance with the later being more active than the former. Another important factor might be NP size, that parameter could be varied in order to find an optimal value. In the same way, calcination temperature and AuCu can be more finely tunned in order to find the optimal structure. One more way to improve the system could be combining the doping of the ceria lattice with Au and Cu (or other dopant) and the deposition of the same bimetallic NP.

Bibliography

[1] Chunwen Sun, Hong Li, and Liquan Chen. Nanostructured ceria-based materials: Synthesis, properties, and applications. *Energy and Environmental Science*, 5(9):8475–8505, 2012.

[2] Dengsong Zhang, Xianjun Du, Liyi Shi, and Ruihua Gao. Shape-controlled synthesis and catalytic application of ceria nanomaterials. *Dalton Transactions*, 41(48):14455–14475, 2012.

[3] Xiaoqiang He, Dengsong Zhang, Hongrui Li, Jianhui Fang, and Liyi Shi. Shape and size effects of ceria nanoparticles on the impact strength of ceria/epoxy resin composites. *Particuology*, 9(1):80–85, 2011.

[4] Yixin Liu, Yu Ding, Lichun Zhang, Pu Xian Gao, and Yu Lei. CeO2 nanofibers for in situ O2 and CO sensing in harsh environments. *RSC Advances*, 2(12):5193–5198, 2012.

[5] Rui Si and Maria Flytzani-Stephanopoulos. Shape and crystal-plane effects of nanoscale ceria on the activity of Au-CeO2 catalysts for the water-gas shift reaction. *Angewandte Chemie - International Edition*, 47(15):2884–2887, 2008.

[6] Anees A. Ansari, S. P. Singh, and B. D. Malhotra. Optical and structural properties of nanostructured CeO2:Tb 3+ film. *Journal of Alloys and Compounds*, 509(2):262–265, 2011.

[7] Xiaohua Liu, Shaojun Chen, and Xiaodong Wang. Synthesis and photoluminescence of CeO 2 :Eu 3+ phosphor powders. *Journal of Luminescence*, 127(2):650–654, 2007.

[8] Alessandro Trovarelli, Carla De Leitenburg, Marta Boaro, and Giuliano Dolcetti. CeO2 in der Katalyse. *Catalysis Today*, 50(2):353–367, 1999.

[9] Jong Hoon Joo and Gyeong Man Choi. Open-circuit voltage of ceria-based thin film SOFC supported on nano-porous alumina. *Solid State Ionics*, 178(29-30):1602–1607, 2007.

[10] Alessandro Trovarelli and Paolo Fornasiero. *Catalysis by Ceria and Related Materials*, volume 12. Imperial College Press, 2013.

[11] Shruba Gangopadhyay, Dmitry D. Frolov, Artëm E. Masunov, and Sudipta Seal. Structure and properties of cerium oxides in bulk and nanoparticulate forms. *Journal of Alloys and Compounds*, 584:199–208, 2014.

[12] Ke Wu, Ling Dong Sun, and Chun Hua Yan. Recent Progress in Well-Controlled Synthesis of Ceria-Based Nanocatalysts towards Enhanced Catalytic Performance. *Advanced Energy Materials*, 6(17):1–46, 2016.

[13] Alessandro Trovarelli. Catalytic properties of ceria and CeO2-Containing materials. *Catalysis Reviews - Science and Engineering*, 38(4):439–520, 1996.

[14] Juan P. Holgado, Rafael Alvarez, and Guillermo Munuera. Study of CeO2 XPS spectra by factor analysis: Reduction of CeO2. *Applied Surface Science*, 161(3):301–315, 2000.

[15] Elisabete C. Moraes Gabriel de Oliveira, Yosio E. Shimabukuro Gabriel de Oliveira, Elisabete C. Moraes, Nathaniel A. Brunsell, Yosio E. Shimabukuro Nathaniel A. Brunsell, , Guilherme A.V. Mataveli Luiz E.O.C. Aragão, Guilherme A.V. Mataveli dos Santos, Thiago V., Thiago V. dos Santos, and Additional information is Ava. Cerium Oxide nanostructures and their Applications. *Intech open*, 2:64, 2015.

[16] Neil J. Lawrence, Joseph R. Brewer, Lu Wang, Tai Sing Wu, Jamie Wells-Kingsbury, Marcella M. Ihrig, Gonghua Wang, Yun Liang Soo, Wai Ning Mei, and Chin Li Cheung. Defect engineering in cubic cerium oxide nanostructures for catalytic oxidation. *Nano Letters*, 11(7):2666–2671, 2011.

[17] E Shoko, M F Smith, and Ross H McKenzie. Charge distribution near bulk oxygen vacancies in cerium oxides. *Journal of Physics: Condensed Matter*, 22(22):223201, 2010.

[18] F. A. Kröger and H. J. Vink. Relations between the Concentrations of Imperfections in Crystalline Solids. *Solid State Physics - Advances in Research and Applications*, 3(C):307–435, 1956.

[19] Michael Nolan, Sonja Grigoleit, Dean C. Sayle, Stephen C. Parker, and Graeme W. Watson. Density functional theory studies of the structure and electronic structure of pure and defective low index surfaces of ceria. *Surface Science*, 576(1-3):217–229, 2005.

[20] S. Tsunekawa, R. Sahara, Y. Kawazoe, and K. Ishikawa. Lattice relaxation of monosize CeO 2-x nanocrystalline particles. *Applied Surface Science*, 152(1):53–56, 1999.

[21] S. Tsunekawa, J. T. Wang, and Y. Kawazoe. Lattice constants and electron gap energies of nano- and subnano-sized cerium oxides from the experiments and first-principles calculations. *Journal of Alloys and Compounds*, 408-412:1145–1148, 2006.

[22] X. D. Zhou and W. Huebner. Size-induced lattice relaxation in CeO2 nanoparticles. *Applied Physics Letters*, 79(21):3512–3514, 2001.

[23] Annapaola Migani, Georgi N. Vayssilov, Stefan T. Bromley, Francesc Illas, and Konstantin M. Neyman. Dramatic reduction of the oxygen vacancy formation energy in ceria particles: A possible key to their remarkable reactivity at the nanoscale. *Journal of Materials Chemistry*, 20(46):10535–10546, 2010.

[24] Alessandro Trovarelli and Jordi Llorca. Ceria Catalysts at Nanoscale: How Do Crystal Shapes Shape Catalysis? *ACS Catalysis*, 7(7):4716–4735, 2017.

[25] Steve Gennard, Furio Corà, and C. Richard A. Catlow. Comparison of the Bulk and Surface Properties of Ceria and Zirconia by ab Initio Investigations. *The Journal of Physical Chemistry B*, 103(46):10158–10170, 2002.

[26] Michael Nolan, Stephen C. Parker, and Graeme W. Watson. The electronic structure of oxygen vacancy defects at the low index surfaces of ceria. *Surface Science*, 595(1-3):223–232, 2005.

[27] Hao Xin Mai, Ling Dong Sun, Ya Wen Zhang, Rui Si, Wei Feng, Hong Peng Zhang, Hai Chao Liu, and Chun Hua Yan. Shape-selective synthesis and oxygen storage behavior of ceria nanopolyhedra, nanorods, and nanocubes. *Journal of Physical Chemistry B*, 109(51):24380–24385, 2005.

[28] Kebin Zhou, Xun Wang, Xiaoming Sun, Qing Peng, and Yadong Li. Enhanced catalytic activity of ceria nanorods from well-defined reactive crystal planes. *Journal of Catalysis*, 229(1):206–212, 2005.

[29] Eleonora Aneggi, Jordi Llorca, Marta Boaro, and Alessandro Trovarelli. Surface-structure sensitivity of CO oxidation over polycrystalline ceria powders. *Journal of Catalysis*, 234(1):88–95, 2005.

[30] Koichi Momma and Fujio Izumi. VESTA 3 for three-dimensional visualization of crystal, volumetric and morphology data. *Journal of Applied Crystallography*, 44(6):1272–1276, 2011.

[31] Mingguang Yao, Xiaobo Du, Hang Lv, Ran Liu, Tian Cui, Zepeng Li, Dongmei Li, Bingbing Liu, Bo Liu, Guangtian Zou, Quanjun Li, Bo Zou, Dedi Liu, and Xu Zou. Facile hydrothermal synthesis of CeO2 nanosheets with high reactive exposure surface. *Journal of Alloys and Compounds*, 509(23):6720–6724, 2011.

[32] Fubo Gu, Zhihua Wang, Dongmei Han, Chen Shi, and Guangsheng Guo. Reverse micelles directed synthesis of mesoporous ceria nanostructures. *Materials Science and Engineering B: Solid-State Materials for Advanced Technology*, 139(1):62–68, 2007.

[33] Kai Lu Yu, Guo Ling Ruan, Yu Heng Ben, and Ji Jun Zou. Convenient synthesis of CeO2 nanotubes. *Materials Science and Engineering B: Solid-State Materials for Advanced Technology*, 139(2-3):197–200, 2007.

[34] Kebin Zhou and Yadong Li. Catalysis based on nanocrystals with well-defined facets. *Angewandte Chemie - International Edition*, 51(3):602–613, 2012.

[35] Jianhui FANG, Zhiyuan CAO, Dengsong ZHANG, Xia SHEN, Weizhong DING, and Liyi SHI. Preparation and CO conversion activity of ceria nanotubes by carbon nanotubes templating method. *Journal of Rare Earths*, 26(2):153–157, 2008.

[36] Chengsi Pan, Dengsong Zhang, and Liyi Shi. CTAB assisted hydrothermal synthesis, controlled conversion and CO oxidation properties of CeO2nanoplates, nanotubes, and nanorods. *Journal of Solid State Chemistry*, 181(6):1298–1306, 2008.

[37] Dengsong Zhang, Chengsi Pan, Liyi Shi, Lei Huang, Jianhui Fang, and Hongxia Fu. A highly reactive catalyst for CO oxidation: CeO2nanotubes synthesized using carbon nanotubes as removable templates. *Microporous and Mesoporous Materials*, 117(1-2):193–200, 2009.

[38] Xusheng Wu and Sibudjing Kawi. Synthesis, growth mechanism, and properties of open-hexagonal and nanoporous-wall ceria nanotubes fabricated via alkaline hydrothermal route. *Crystal Growth and Design*, 10(4):1833–1841, 2010.

[39] Yifu Yu, Yingming Zhu, and Ming Meng. Preparation, formation mechanism and photocatalysis of ultrathin mesoporous single-crystal-like CeO 2 nanosheets. *Dalton Transactions*, 42(34):12087–12092, 2013.

[40] Bert Freitag, Kenji Kaneko, Satoshi Ohara, Jing Zhang, Ana B. Hungria, Paul A. Midgley, Koji Inoke, Tadafumi Adschiri, and Thomas W. Hansen. Structural and Morphological Characterization of Cerium Oxide Nanocrystals Prepared by Hydrothermal Synthesis. *Nano Letters*, 7(2):421–425, 2007.

[41] Yan Liu, Zhaochi Feng, Can Li, Emiel J. M. Hensen, Haidong Zhang, and Yejun Guan. Template-Free Synthesis of Sphere, Rod and Prism Morphologies of CeO2 Oxidation Catalysts. *Catalysis Letters*, 137(1-2):28–34, 2010.

[42] Lluís Soler, Albert Casanovas, Aitor Urrich, Inmaculada Angurell, and Jordi Llorca. CO oxidation and COPrOx over preformed Au nanoparticles supported over nanoshaped CeO2. *Applied Catalysis B: Environmental*, 197:47–55, 2016.

[43] C. T. Rettner, D. J. Auerbach, J. C. Tully, and A. W. Kleyn. Chemical dynamics at the gas-surface interface, 1996.

[44] Yuichiro Murata, Keita Ikeue, Masato Machida, Kouji Kishikawa, and Dongjie Zhang. On the Reasons for High Activity of CeO 2 Catalyst for Soot Oxidation . *Chemistry of Materials*, 20(13):4489–4494, 2008.

[45] Guomin Hua, Lide Zhang, Guangtao Fei, and Ming Fang. Enhanced catalytic activity induced by defects in mesoporous ceria nanotubes. *Journal of Materials Chemistry*, 22(14):6851–6855, 2012.

[46] Xin Song Huang, Hao Sun, Lu Cun Wang, Yong Mei Liu, Kang Nian Fan, and Yong Cao. Morphology effects of nanoscale ceria on the activity of Au/CeO2 catalysts for low-temperature CO oxidation. *Applied Catalysis B: Environmental*, 90(1-2):224–232, 2009.

[47] Wenjie Shen, Santhosh Chenna, Yong Li, Na Ta, Peter A. Crozier, Jingyue (Jimmy) Liu, and Aling Chen. Stabilized Gold Nanoparticles on Ceria Nanorods by Strong Interfacial Anchoring. *Journal of the American Chemical Society*, 134(51):20585–20588, 2012.

[48] Hyun You Kim, Hyuck Mo Lee, and Graeme Henkelman. CO oxidation mechanism on CeO 2-supported Au nanoparticles. *Journal of the American Chemical Society*, 134(3):1560–1570, 2012.

[49] Silvia Carrettin, Patricia Concepción, Avelino Corma, José M. López Nieto, and Victor F. Puntes. Nanocrystalline CeO2increases the activity of Au for CO oxidation by two orders of magnitude. *Angewandte Chemie - International Edition*, 43(19):2538–2540, 2004.

[50] Guangquan Yi, Zhongning Xu, Guocong Guo, Ken ichi Tanaka, and Youzhu Yuan. Morphology effects of nanocrystalline CeO2 on the preferential CO oxidation in H2-rich gas over Au/CeO2 catalyst. *Chemical Physics Letters*, 479(1-3):128–132, 2009.

[51] Shuang Liu, Xiaodong Wu, Wei Liu, Wenming Chen, Rui Ran, Min Li, and Duan Weng. Soot oxidation over CeO2and Ag/CeO2: Factors determining the catalyst activity and stability during reaction. *Journal of Catalysis*, 337:188–198, 2016.

[52] Matteo Farnesi Camellone and Stefano Fabris. Reaction mechanisms for the CO oxidation on Au/CeO2 catalysts: Activity of substitutional Au3+/Au+ cations and deactivation of supported Au+ adatoms. *Journal of the American Chemical Society*, 131(30):10473–10483, 2009.

[53] X. Lai, D.W. Goodman, and M. Valden. Onset of Catalytic Activity of Gold Clusters on Titania with the Appearance of Nonmetallic Properties. *Science*, 281(5383):1647–1650, 1998.

[54] Parthasarathi Bera and M. S. Hegde. Characterization and catalytic properties of combustion synthesized Au/CeO2 catalyst. *Catalysis Letters*, 79(1-4):75–81, 2002.

[55] Alberto Sandoval, Catherine Louis, and Rodolfo Zanella. Applied Catalysis B : Environmental Improved activity and stability in CO oxidation of bimetallic Au – Cu / TiO 2 catalysts prepared by deposition – precipitation with urea. *Applied Catalysis B: Environmental*, 141:363–377, 2013.

[56] Sharif Najafishirtari, Rosaria Brescia, Pablo Guardia, Sergio Marras, Liberato Manna, and Massimo Colombo. Nanoscale Transformations of Alumina-Supported AuCu Ordered Phase Nanocrystals and Their Activity in CO Oxidation. *ACS Catalysis*, 5(4):2154–2163, 2015.

[57] Aiqin Wang, Xiao Yan Liu, Chung Yuan Mou, and Tao Zhang. Understanding the synergistic effects of gold bimetallic catalysts. *Journal of Catalysis*, 308:258–271, 2013.

[58] Xiaoyan Liu, Aiqin Wang, Lin Li, Tao Zhang, Chung Yuan Mou, and Jyh Fu Lee. Structural changes of Au-Cu bimetallic catalysts in CO oxidation: In situ XRD, EPR, XANES, and FT-IR characterizations. *Journal of Catalysis*, 278(2):288–296, 2011.

[59] Thiago S. Mozer, Dominika A. Dziuba, Carlos T.P. Vieira, and Fabio B. Passos. The effect of copper on the selective carbon monoxide oxidation over alumina supported gold catalysts. *Journal of Power Sources*, 187(1):209–215, 2009.

[60] M. Stan, Y. T. Zhu, H. Jiang, and D. P. Butt. Kinetics of oxygen removal from ceria. *Journal of Applied Physics*, 95(7):3358–3361, 2004.

[61] Nicole Knoblauch, Lars Dörrer, Peter Fielitz, Martin Schmücker, and Günter Borchardt. Surface controlled reduction kinetics of nominally undoped polycrystalline CeO2. *Physical Chemistry Chemical Physics*, 17(8):5849–5860, 2015.

[62] Jordi Llorca, Montserrat Domínguez, Cristian Ledesma, Ricardo J. Chimentão, Francisco Medina, Jesús Sueiras, Inmaculada Angurell, Miquel Seco, and Oriol Rossell. Propene epoxidation over TiO2-supported Au-Cu alloy catalysts prepared from thiol-capped nanoparticles. *Journal of Catalysis*, 258(1):187–198, 2008.

[63] John F.Watts and John Wolstenholme. *An introduction to Surface Analysis by XPS and AES*. Wiley, 2003.

[64] S. Tanuma, H. Yoshikawa, H. Shinotsuka, and R. Ueda. Calculations of mean escape depths of photoelectrons in elemental solids excited by linearly polarized X-rays for high-energy photoelectron spectroscopy. *Journal of Electron Spectroscopy and Related Phenomena*, 190(PART B):127–136, 2013.

[65] S. Tanuma, C. J. Powell, and D. R. Penn. Calculations of electorn inelastic mean free paths. II. Data for 27 elements over the 50–2000 eV range. *Surface and Interface Analysis*, 17(13):911–926, 1991.

[66] Hanbin Liao, Adrian Fisher, and Zhichuan J. Xu. Surface Segregation in Bimetallic Nanoparticles: A Critical Issue in Electrocatalyst Engineering. *Small*, 11(27):3221–3246, 2015.

[67] Priscila Destro, Tathiana M Kokumai, Alice Scarpellini, Lea Pasquale, Liberato Manna, Massimo Colombo, and Daniela Zanchet. The Crucial Role of the Support in the Transformations of Bimetallic Nanoparticles and Catalytic Performance. *ACS Catalysis*, 8(2):1031–1037, 2018.

[68] Asunción Aranda, Said Agouram, Jose M. López, Ana M. Mastral, David R. Sellick, Benjamín Solsona, Stuart H. Taylor, and Tomás García. Oxygen defects: The key parameter controlling the activity and selectivity of mesoporous copper-doped ceria for the total oxidation of naphthalene. *Applied Catalysis B: Environmental*, 127:77–88, 2012.

[69] Hyung Jun Kim, Geonhee Lee, Myeong Gon Jang, Kyung Jong Noh, and Jeong Woo Han. Rational Design of Transition Metal Co-doped Ceria Catalysts for Low-Temperature CO Oxidation. *ChemCatChem*, pages 2288–2296, 2019.

[70] Jose Garcia-Torres, Elisa Vallés, and Elvira Gómez. Synthesis and characterization of Co@Ag core-shell nanoparticles. *Journal of Nanoparticle Research*, 12(6):2189–2199, 2010.

[71] Baolin Liu, Yizhao Li, Yali Cao, Lei Wang, Shaojun Qing, Kun Wang, and Dianzeng Jia. Optimum Balance of Cu + and Oxygen Vacancies of CuO x -CeO 2 Composites for CO Oxidation Based on Thermal Treatment. *European Journal of Inorganic Chemistry*, 2019(13):1714–1723, 2019.

[72] Marcello Marelli, Andrea Jouve, Alberto Villa, Rinaldo Psaro, Antonella Balerna, Laura Prati, and Claudio Evangelisti. Hybrid Au/CuO Nanoparticles: Effect of Structural Features for Selective Benzyl Alcohol Oxidation. *Journal of Physical Chemistry C*, 123(5):2864–2871, 2019.

[73] C.D Wagner, W.M. Riggs, L.E. Davis, J.F. Moulder, and G.E. Muilenberg. Handbook of X-Ray Photoelectron Spectroscopy.pdf.

[74] Claudio Sangregorio, Monica Galeotti, Ugo Bardi, and Piero Baglioni. Synthesis of Cu 3 Au Nanocluster Alloy in Reverse Micelles. *American Chemical Society*, 7463(96):5800–5802, 1996.

[75] Min Joo Kim, Heay Jin Na, Kyoung Chul Lee, Eun Ah Yoo, and Minyung Lee. Preparation and characterization of Au-Ag and Au-Cu alloy nanoparticles in chloroform. *Journal of Materials Chemistry*, 13(7):1789–1792, 2003.

[76] Gongwei Wang, Li Xiao, Bing Huang, Zhandong Ren, Xun Tang, Lin Zhuang, and Juntao Lu. AuCu intermetallic nanoparticles: Surfactant-free synthesis and novel electrochemistry. *Journal of Materials Chemistry*, 22(31):15769–15774, 2012.

[77] Claudia. Sánchez. Detección y caracterización molecular de los parásitos de interés en salud pública: Giardia duodenalis, Cryptosporidium spp., Cyclospora cayetanensis, Toxoplasma gondii y Entamoeba histolytica, en agua cruda y tratada de cuatro plantas potabilizadoras del. *Surface and Interface Analysis*, 4(0):0–1, 2017.

[78] Isabel Barroso-Martín, Elisa Moretti, Aldo Talon, Loretta Storaro, Enrique Rodríguez-Castellón, and Antonia Infantes-Molina. Au and AuCu nanoparticles supported on SBA-15 ordered mesoporous titania-silica as catalysts for methylene blue photodegradation. *Materials*, 11(6):1–17, 2018.

[79] The Ce, The Ce, National Synchrotron, and Light Source. Electron Spectroscopy of Single Crystal and Polycrystalline Cerium Oxide Surfaces Surface Science , 409 (1998) 307. *Surface Science*, 409(1998):3–5, 2014.

[80] A Pfau and K D Schierbaum. Pfau, Schierbaum - The electronic structure of stoichiometric and reduced CeO, surfaces an XPS, UPS and HREELS study - 1994 - Surface Science.pdf. *Surface Science*, 6028(94), 1994.

[81] G. Praline, B. E. Koel, R. L. Hance, H. I. Lee, and J. M. White. X-Ray photoelectron study of the reaction of oxygen with cerium. *Journal of Electron Spectroscopy and Related Phenomena*, 21(1):17–30, 1980.

[82] Mark C. Biesinger, Brad P. Payne, Andrew P. Grosvenor, Leo W.M. Lau, Andrea R. Gerson, and Roger St C. Smart. Resolving surface chemical states in XPS analysis of first row transition metals, oxides and hydroxides: Sc, Ti, V, Cu and Zn. *Applied Surface Science*, 257(7):2717–2730, 2011.

[83] Feng Tao, Michael E Grass, Yawen Zhang, Derek R Butcher, James R Renzas, Zhi Liu, Jen Y Chung, Bongjin S Mun, Miquel Salmeron, and Gabor A Somorjai. Reaction-Driven Restructuring of Rh-Pd and Pt-Pd Core-Shell Nanoparticles. *Science*, 322(November):932–935, 2008.

[84] Shend Dai Zhen Ma. *Heterogeneous Gold Catalysts and Catalysis Series Editors :*. Royal Society of CHemistry, 2014.

[85] Liang Zhang, Hyun You Kim, and Graeme Henkelman. CO oxidation at the Au-Cu interface of bimetallic nanoclusters supported on CeO2(111). *Journal of Physical Chemistry Letters*, 4(17):2943–2947, 2013.

Appendix

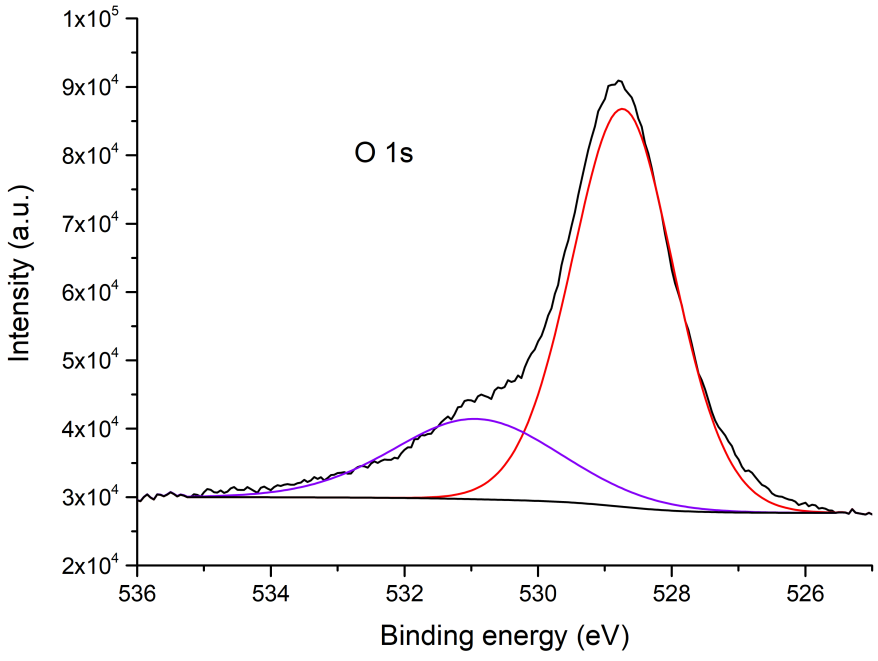

Figure 15: Pre-reaction XPS spectrum showing O 1s.

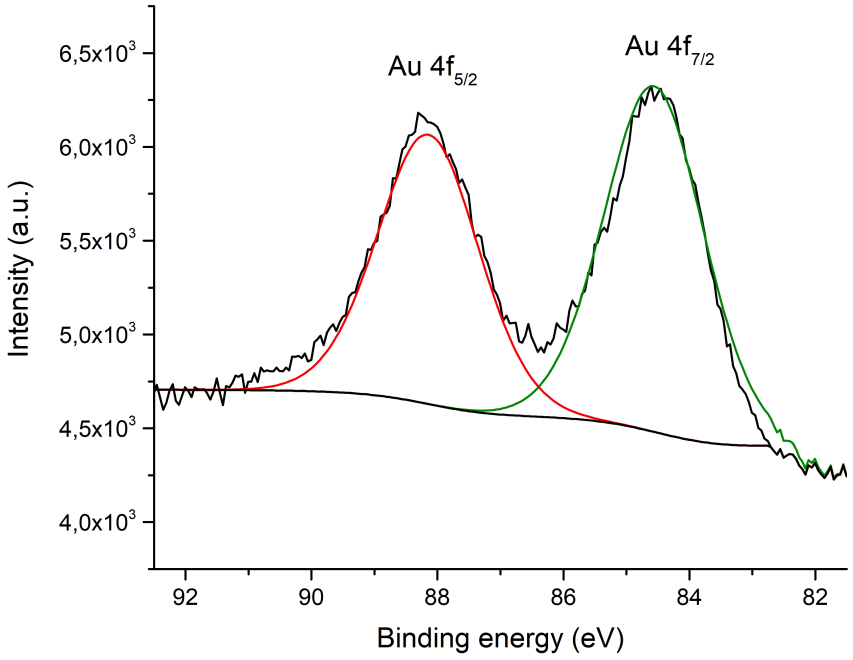

Figure 16: XPS spectrum showing Au 4f doublet. In black is presented the photoelectron intensity and in red and green the deconvolution of the data.

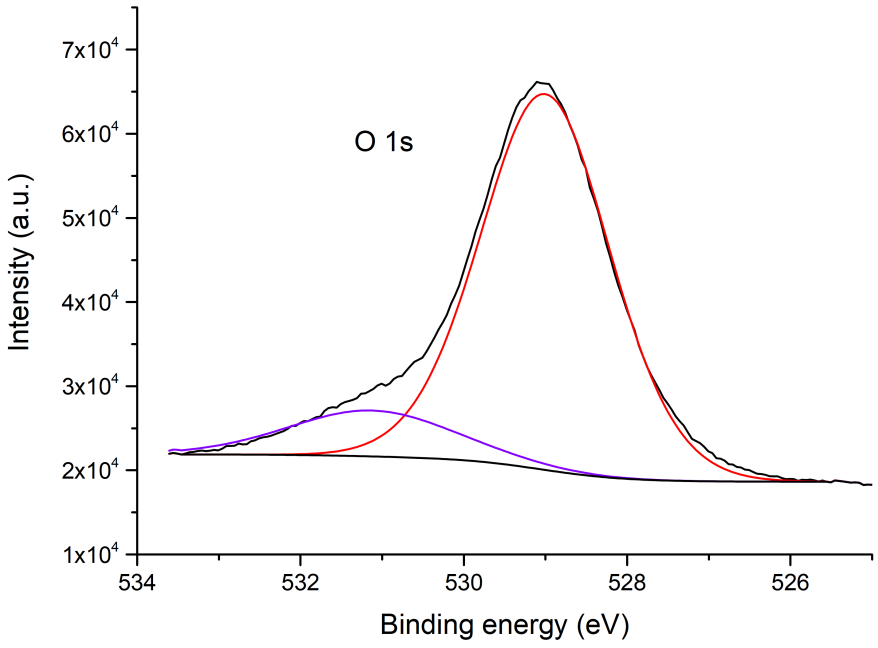

Figure 17: Post-reaction XPS spectrum showing O 1s.

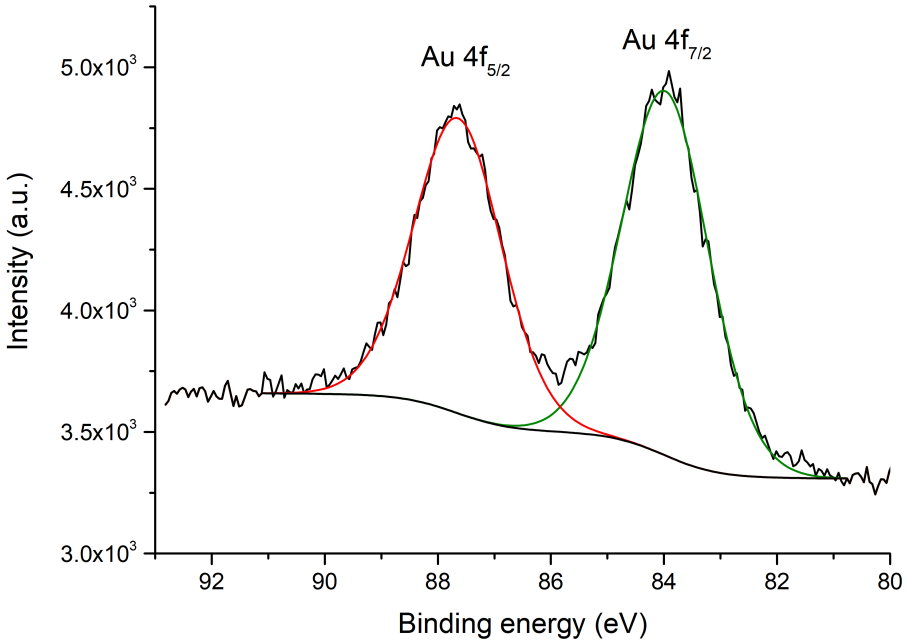

Figure 18: Post-reaction XPS spectrum showing Au 4f doublet.